Characteristics of quasi-stationary near-wall turbulence subjected to strong stable stratification in open-channel flows

Amir Atoufi* and K. Andrea Scott
Department of Systems Design Engineering, University of Waterloo, Waterloo, Ontario N2L 3G1, Canada

Michael L Waite
Department of Applied Mathematics, University of Waterloo, Waterloo, Ontario N2L 3G1, Canada
(Dated: May 28, 2021)

Characteristics of near-wall turbulence at quasi-stationarity under strong wall cooling are studied using direct numerical simulation of open-channel flow. It is shown that if turbulence reaches quasi-stationarity, the characteristics of quasi-stationary near-wall turbulence, even with the strongest wall cooling rate, are generally similar to the weakly stratified case. The effects of strong stable stratification on the characteristics of near-wall turbulence are transient. The effect of stratification on several characteristics of stratified near-wall turbulence, including first, second and higher-order statistics, turbulent kinetic energy budget, and mechanisms involved in the evolution of turbulence producing eddies, are discussed. It is shown that among mechanisms that contribute to the budget of turbulent kinetic energy, transfer and pressure-work are more dependent on the stratification if turbulence reaches quasi-stationarity. The buoyancy destruction term influences the budget for the tangential Reynolds stress more than the budget for the turbulent kinetic energy. Relevant length scales are also discussed in detail. The Corrsin and Ellison scales are smaller than the Ozmidov scales and are sensitive to stratification in the upper logarithmic layer and in the outer layer. The Corrsin scales in the lower half of the buffer layer and fine scales structures of wall-normal velocity in the viscous sublayer are smaller than the Kolmogorov scale. Finally, the effect of heat entrainment from the upper boundary and computational domain size are also examined. In summary, it is found the behaviour of near-wall turbulence at quasi-stationarity is approximately similar to weakly stratified cases, regardless of the choice of upper boundary condition.

I. INTRODUCTION

In the stably stratified atmospheric boundary layer (ABL), the reduction of vertical mixing has a significant effect from an environmental perspective. For example, the reduced vertical mixing with stable stratification may lead to increased air pollution by a localized accumulation of black carbon [1] and a considerable reduction in power output from large wind farms [2]. Turbulence in the stably stratified ABL involves complexities such as spatio-temporal intermittency [3–9], microfronts [6, 10], and gravity wave breaking [6, 11], which are not yet completely understood. These complexities can be studied by simulating stably-stratified wall-bounded shear-flow (e.g. stratified channel flows) as an idealized model for the stable atmospheric boundary layer.

For such idealized models, wall-modelled LES studies of the ABL in rotating reference frames [12] have shown that an increase in stable stratification leads to stronger vertical gradients of the mean temperature, a decrease in vertical turbulent momentum flux, an increase in vertical turbulent temperature flux, and a ABL that is typically shallower [12, 13]. The integral length scale and turbulence production decrease as stratification increases [12].

The effects of stratification on the budget of turbulent kinetic energy (TKE) have been studied for quasi-stationary turbulence with LES [14–16] and non-stationary turbulence with direct numerical simulations (DNS) [3, 4, 17–19]. Furthermore, the recent experimental study of

* aatoufi@uwaterloo.ca

Williams *et. al* [13] of stably stratified turbulence over a flat plate has shown that increasing stratification is associated with strong reductions in tangential Reynolds stress, leading to the collapse of turbulence production by mean shear. The motions that contribute to negative Reynolds stress and positive turbulence production due to mean shear (Q2 and Q4 events [20, 21]) are most affected by stratification. The ejections (Q2) are damped and sweeps (Q4) are not significantly affected by stable stratification. The motions that contribute to positive tangential Reynolds stress and negative production ($Q1$ and $Q3$ events) are less affected.

Taylor *et. al* [16] performed an LES study of open channel flow at friction Reynolds number $Re_\tau = 400$ with imposed negative density gradient at the top and zero density gradient at the bottom for relatively weak stratification up to friction Richardson number $Ri_\tau = 500$ and Prandtl number $Pr = 5$. The velocity fluctuations in the inner layer of the bottom boundary layer are not significantly influenced by stratification in their results. This minimal dependence of near-wall velocity fluctuations on stratification raises a question regarding the location of the imposed density gradient. If the density gradient (source of strongly stable stratification) were placed on the bottom wall, which is where the turbulence is generated by shear, would the turbulence be more affected by the stratification? Here, we address this question for open channel flow at quasi-stationarity, which was also the state investigated in Taylor *et. al* [16]. While there are a number of relatively recent DNS studies that have also addressed this question, these studies used either a closed channel [5, 9] or an open channel with fixed top temperature [8, 19, 22, 23]. From the perspective of a nocturnal ABL, an open channel is the more relevant idealized case. In the latter studies, stratification is imposed on both the bottom wall and the upper boundary. However, these latter studies did not discuss characteristics of the strongly stable regime. By strongly stable, we mean stratification that is strong enough to cause intermittency or full collapse and relaminarization of fully developed turbulence shortly after stratification is introduced; this perspective is motivated by earlier experimental [13, 24] and numerical studies [5, 8, 9].

In the case of strong stable stratification, an important question is how strongly stratified turbulence that recovers from possible collapse compares to weakly or neutrally stratified wall-bounded turbulence.

Apart from bottom cooling, heat entrainment from the upper boundary layer for strong stable stratification can significantly affect boundary layer dynamics as a result of the strong capping inversion [22, 23, 25, 26] that develops beneath the top boundary[4]. In the real nocturnal ABL the capping inversion controls the boundary layer height [25]. It is therefore also important to address the impact of heat flux from the upper boundary on the characteristics of wall-bounded turbulence. In realistic flows, due to active momentum transfer from the free atmosphere into ABL, heat may be entrained into the ABL [27]. In our open-channel flow simulations with a rigid lid at top boundary, we used heat entrainment to refer to heat flux from top boundary.

Here, we mainly examine the quasi-stationary state, which may nevertheless inform our perception of evolving stable boundary layers, which are usually complicated by the dependence of the turbulence statistics upon time. The main themes of the present work are as follows: 1) characterizing first and second-order statistics and relevant length scales of wall-generated turbulence under strong stable stratification at a quasi-stationarity state with a focus on the near-wall region where turbulence has been shown to be largely affected by buoyancy earlier in the surface cooling process [4], 2) investigating the impact of a capping inversion, and 3) analyzing sensitivity to the choice of computational domain size. The rest of the paper is divided into three sections. In Sec. II, the governing equations are presented and the numerical approach is briefly discussed. The results are shown in Sec. III. The notion of "strong stable" stratification is first discussed in the context of the current study in Sec. III A.

We then study the effect of stratification on the first and second-order statistics and TKE in Sec. III B. Then, mixing and stratification effects are diagnosed using non-dimensional numbers in Sec. III C. The TKE budget is presented and discussed in Sec. III D. Kinetic energy redistribution is addressed in Sec. III E. After studying the TKE budget, turbulence production is explored in Sec. III F. Typical length scales for stratified wall-bounded turbulence are introduced and investigated in Sec. III G and in Sec. III H. Higher-order statistics are examined in Sec. III I. The results section concludes by reviewing the sensitivity of some of the diagnostics to heat entrainment from the upper boundary in Sec. III J and computational domain size in Sec. III K. The paper ends with conclusions in Sec. IV.

II. GOVERNING EQUATIONS AND METHODOLOGY

In this work, the non-dimensional Navier-Stokes equations under the Oberbeck-Boussinesq approximation (OBA) are used. With the choice of channel height, reference friction velocity, and a value for the imposed bottom-surface temperature gradient, the dimensionless OBA equations can be written as [5, 16]

$$\frac{\partial u_i}{\partial x_i} = 0, \tag{1}$$

$$\frac{\partial u_i}{\partial t} + u_j \frac{\partial u_i}{\partial x_j} = -\frac{\partial p}{\partial x_i} + \frac{1}{Re_\tau} \frac{\partial^2 u_i}{\partial x_j \partial x_j} + Ri_\tau \; \theta \; \delta_{i3} + \delta_{i1}, \tag{2}$$

$$\frac{\partial \theta}{\partial t} + u_j \frac{\partial \theta}{\partial x_j} = \frac{1}{Pr Re_\tau} \frac{\partial^2 \theta}{\partial x_j \partial x_j}, \tag{3}$$

where Re_τ, Ri_τ, and Pr are reference friction Reynolds, Richardson and Prandtl numbers. The variables u_i, θ, and p are the ith velocity component, deviation of the temperature field from the constant background temperature, and deviation of the pressure from the hydrostatic background pressure. $(u_1, u_2, u_3) = (u, v, w)$ are the component of velocity in the streamwise, spanwise, and wall-normal directions, which correspond to the x, y, and z axes of the Cartesian coordinate system, respectively.

The open-source flow solver Hercules [5] is used to solve the governing equations numerically. This model employs the Fourier-spectral method in the horizontal directions along with second-order finite difference and grid staggering in the vertical direction. Grid stretching is also used in vertical direction where the mesh is denser close to bottom to resolve small scales near the wall. For dealising, Fourier modes are truncated following the 2/3 rule in the horizontal directions, and a skew-symmetric form of nonlinear advection terms is employed in the vertical direction [28]. Continuity is enforced by applying the fractional step method [29].

A constant force is included in the x momentum equation to drive flow in the x-direction. Periodic boundary conditions have been employed in the horizontal (x-y) plane while no-slip and free-slip boundary condition are applied at the wall and at channel top, respectively. The temperature boundary condition at the bottom boundary is Neumann with $\partial\theta/\partial z = 1$ to impose surface cooling and stable stratification. Two types of boundary conditions are considered for the temperature of the upper boundary: Neumann ($\partial\theta/\partial z = 0$) for the main simulations, where the upper boundary is adiabatic, and Dirichlet ($\theta = 0$) for additional cases that include heat flux at the upper boundary.

Five main high-resolution simulations (C1-C5) with $Re_\tau = 560$ are performed in this study, as presented in Table I. For these simulations the domain size is $L_x = 2\pi$, $L_y = \pi$, and $h = 1$ and grid spacings based on wall units are $\Delta x^+ = 4.6$, $\Delta y^+ = 2.3$ in horizontal directions, and $\Delta z^+ \in [0.08 - 3.3]$ in the vertical. Plus unit are scaled by Reynolds number, e.g. $\Delta z^+ = \Delta z \; Re_\tau$. Simulations include one unstratified case (C1) and four stratified cases (C2-C5), with Ri_τ ranging from 0 to 1120. The

time step is $\Delta t = 0.0002$ in C1 and C2 and $\Delta t = 0.00015$ for C3-C5. The stratified cases C2-C5 are initialized from an output of the neutral case C1 within the quasi-stationarity state. The unstratified case is run for a total of 53 outer layer time units $t^d = t/t^o$, where $t^o = h/u_\tau$ is in order of the time scales of the outer layer eddies and u_τ is the friction velocity based on the value of the mean shear at the wall and h is the channel height. After initialization, cases C2, C3, C4, and C5 are run for 49, 48, 55, and 62 outer layer unit times, respectively.

The temporal evolution of TKE $k = \overline{u_i' u_i'}/2$, where $u_i' = u_i - \overline{u}_i$ and mean kinetic energy (MKE) $K = \overline{u}_i \overline{u}_i/2$ integrated over the domain are shown in Fig. 1 for C1-C5. Overbar denotes averaging over horizontal directions and time throughout this paper (except for explicitly stated quantities that are time dependant, for which overbar denotes horizontal averaging only). It can be seen that, during the last 12 time units, a quasi-stationary state is reached for the cases considered here. Therefore the reported quantities in this study are averaged over the last 12 time units. Moreover, as shown in Fig. 1, the stratified cases take more time to reach quasi-stationarity due to the increase of flow time scales caused by stable stratification [4].

Note that the qualifier "quasi" is used since the domain-averaged temperature decreases due to the boundary conditions [16, 18](pure cooling) for C2-C5 and does not reach stationarity. Nevertheless, this decrease does not affect the buoyancy frequency, mean velocities, and fluctuating fields, which all appear stationary as shown in Fig. 1 [4].

Additional simulations are performed to investigate the effect of very strong stratification (C6), computational domain size (C5DC, L5D) and the upper thermal boundary condition (C2D, C5D). Turbulence in case C6 collapses and does not recover (Fig. 1), which shows that Ri_τ in C5 is approximately the maximum at which near wall turbulence may recover to quasi-stationarity. This case is run for 30 outer layer unit times. For C5DC and L5D $\Delta x^+ = 9.2$, $\Delta y^+ = 4.6$, and $\Delta z^+ \in [0.32 - 6.3]$. For cases C2D, C5D, and C6, the same grid spacings as in C1-C5 are used. For C2D, C5D, and C6, the time step is $\Delta t = 0.00015$, while $\Delta t = 0.0003$ is used for C5DC and L5D. The case C5DC is initialized by sampling the output of C5D at the time TKE become quasi-stationary on a grid that is two times coarser in each direction. Using the output of C5DC at quasi-stationarity, case L5D is initialized by periodically extending the output of C5DC by 8 times in the streamwise direction and 6 times in the spanwise direction. The BC column in Table I refers to the choice of upper thermal boundary condition where N refers to Neumann ($\partial\theta/\partial z = 0$) and D refers to Dirichlet ($\theta = 0$). The latter leads to entrainment of heat from the upper boundary.

The h/L_{MO} in Table I refers to the ratio of Monin-Obukhov scale to channel height, where the MO scale L_{MO} is (in terms of dimensionless quantities)

$$\frac{L_{MO}}{h} = \frac{Re_\tau Pr}{\kappa Ri_\tau}, \tag{4}$$

and $\kappa \approx 0.41$ is the von Kármán constant. More details for simulations C1-C5 are given in Atoufi *et. al* [4]. All parameters and diagnostic quantities are dimensionless.

III. RESULTS

A. Strength of Stratification

Before we discuss the results, let us clarify what we mean by "strong stable stratification" within the context of the current study, as we often use this terminology. The classification of stable stratification regimes in this work, as a result of wall cooling, is determined by the transient state. The time evolution of cases C1-C6 in Fig. 1 show that distinct phases exist in the cooling process, which we discuss in detail in [4]. These cases undergo an initial decay that lasts for 4-6 (outer layer eddy) turnover times, where the longest decay phase corresponds to the strongest stable case, C6, considered here. The next phase is recovery, when turbulence re-

TABLE I. Parameters of simulations

Case	Re_τ	Ri_τ	h/L_{MO}	L_x/h	L_y/h	t_f	BC	N_x	N_y	N_z
C1	560	0	0	2π	π	53.2	N/N	768	768	384
C2	560	560	0.41	2π	π	48.5	N/N	768	768	384
C3	560	697	0.51	2π	π	47.7	N/N	768	768	384
C4	560	833	0.61	2π	π	55.19	N/N	768	768	384
C5	560	1120	0.82	2π	π	62.6	N/N	768	768	384
C6	560	2800	2.05	2π	π	30.9	N/N	768	768	384
C2D	560	560	0.41	2π	π	40	N/D	768	768	384
C5D	560	1120	0.82	2π	π	60	N/D	768	768	384
C5DC	560	1120	0.82	2π	π	140.8	N/D	384	384	192
L5D	560	1120	0.82	8π	6π	70.9	N/D	1536	2304	192

covers from the initial decay caused by the stable stratification. The recovery phase is generally longer than the decay phase, and simulations with higher Ri_τ take longer to recover from the initial decay. For instance, the recovery phase for C5 is $4 \lesssim tu_\tau^0/h \lesssim 45$, which highlights the significance of stable stratification in increasing the time scale of the energy-containing eddies during the decay phase.

The recovery of the more strongly stratified cases C4 and C5 behave differently when compared to the more weakly stratified cases C1-C3, which suggests that C4 and C5 are in a different stable stratification regime. In these two cases, the domain integrated MKE and TKE (Fig. 1) show an overshoot in the recovery phase of the cooling process, which is different from C2 and C3 where quasi-stationarity is asymptotically approached without such overshoots. Moreover, for C4 and C5, the initial decay of TKE (Fig. 1b) is larger than C2 and C3. In particular, in C5, the effect of stratification is strong enough to cause partial collapse of turbulence for almost 20 turnover times. Due to these differences, we mark stratification regime for C4 and C5 as strongly stable. In C6, stratification is so strong that the flow does not recover to a turbulent state and fully collapses.

The Ri_τ for C5 and C6 lie in the region of strongly-stratified turbulence in the $(Re_\tau - Ri_\tau)$ space diagram for stably stratified wall-bounded flows given by Zonta and Soldati [7] based on previous DNS studies.

Flores and Riley [8] also simulated open-channel flow with the same parameters and bottom boundary condition as in C5 and used a Dirichlet boundary condition at top. They found the stratification in this case to be strong enough to cause intermittency. However, and as we will show in this study, despite the fact that the impact of stratification on the flow is strong in the decay and recovery phase, when quasi-stationarity is reached, the impact of stratification is weak.

The friction coefficient is defined as the ratio of the wall shear stress to the kinetic energy of the bulk flow and is expressed as [16]

$$C_f = \frac{2\tau_w}{\rho u_b^2} = \frac{2u_\tau^2}{u_b^2}, \tag{5}$$

where $u_b = \frac{1}{h}\int_0^h \overline{u}\ \mathrm{d}z$ is the bulk flow velocity and overbar refers to averaging over the horizontal plane. Time series of the friction coefficient are shown in Fig. 1(d). The friction coefficient monotonically decreases with increasing surface cooling rate (increasing Ri_τ), consistent with other studies of stably stratified boundary layers [13, 15, 16]. Similar to TKE, C_f also undergoes a rapid decay followed by recovery to a quasi-stationary value for each case. The C_f values for C6 also shows drastic decrease and no signs of recovery consistent will full collapse of turbulence across whole boundary layer.

Before discussing the quasi-stationary state,

it should be noted that whether the turbulence collapses or not, and the Ri_τ at which collapse occurs, is also sensitive to the choice of initial condition. For example, for a case with $Ri_\tau = 1680$ (with parameters and boundary condition similar to C5), initialization using a neutral case at the same Re_τ leads to full collapse. However if the simulation is initialized using output from C5 at quasi-stationarity state when $tu_\tau^0/h = 23.7$, plus uniformly distributed random noise in the velocity field with zero mean and variance of 0.2, turbulence recovers and attains quasi-stationarity state.

B. First- and second-order statistics

In this section, we focus on the overall effect of stratification on characteristics of the quasi-stationary state for simulations C1-C5. The mean velocity profile is shown in Fig. 2a. Increasing stratification (i.e. by increasing the bottom wall cooling flux by increasing Ri_τ) increases the mean velocity above the buffer layer at $z^+ \gtrsim 30$; as will be shown below, this is a result of flow acceleration due to the decrease in wall shear stress (Fig. 6a). All cases exhibit log-linear behaviour of mean velocity for $30 \lesssim z^+ \lesssim 100$ with a monotonic increase of the slope of the log-linear profile as Ri_τ increases. The mean velocity up to the end of the buffer region ($z^+ \lesssim 30$) is almost independent of stratification.

Profiles of the buoyancy frequency N^2, where

$$N^2 = Ri_\tau \frac{\partial \overline{\theta}}{\partial z}, \tag{6}$$

are shown in Fig. 2(b). In contrast to the mean velocity profiles, the effect of the cooling flux on the mean temperature gradient is greatest near the lower boundary. As expected, increasing Ri_τ results in monotonic enhancement of N^2 near the wall, which becomes weaker moving upward. However, the dependence of N^2 upon Ri_τ is much less pronounced above $z^+ = 100$. Therefore, for C2-C5, the buoyancy restoring force, which increases with Ri_τ, is strongest at lower boundary and becomes weakest at the upper boundary.

One-point statistics of velocity fluctuations are shown in Fig. 3, and TKE is shown in Fig. 4. Generally, and similar to studies of weakly stratified cases [16], all cases show similar profiles in the inner layer for $z \lesssim 0.2$ ($z^+ \leq 100$) and slightly different trends in the outer layer $z \gtrsim 0.2$ ($z^+ > 100$). For example, $\overline{u'^2}$ and $\overline{v'^2}$ above $z > 0.6$ decrease slightly as Ri_τ increases. The decrease in $\overline{w'^2}$ with increasing stratification is consistent across the channel height.

The dominant contribution to TKE for $z \lesssim 0.1$ comes from $\overline{u'^2}$. Specifically, almost 85% of the TKE peak in the near-wall region comes from the streamwise velocity fluctuations. The maximum of this streamwise fraction of the TKE in the buffer region is reduced as stratification increases (zoomed-in box in Fig. 3a). However, above $z \approx 0.2$ the $\overline{u'^2}$ contribution is reduced to about 50% where the $\overline{v'^2}$ and $\overline{w'^2}$ contributions increase and reach about 30% and 20% of total TKE respectively up to $z \approx 0.9$.

Although the mean velocity profiles show clear differences, even in the buffer layer (Fig. 2a), the maxima of the velocity fluctuations with stratification are within 10% of those from the neutral case. The result here are consistent with the study of Taylor *et. al* [16] although we have used different boundary conditions by imposing the source of stable stratification on the bottom wall where turbulence is generated.

This degree of similarity between velocity fluctuations for different stratifications, even in the most strongly stable quasi-stationary case C5, for which turbulence partially collapsed at an earlier stage of the cooling process [4], strongly supports the idea that the destruction of TKE by stable stratification is a transient process as also discussed in Donda *et. al* [22, 23]. If turbulence passes the decay and recovery phases [4], the quasi-stationary characteristics of near-wall turbulence are generally similar to the weakly stratified case. This transient effect will be further discussed when the budget of TKE and tangential Reynolds stresses

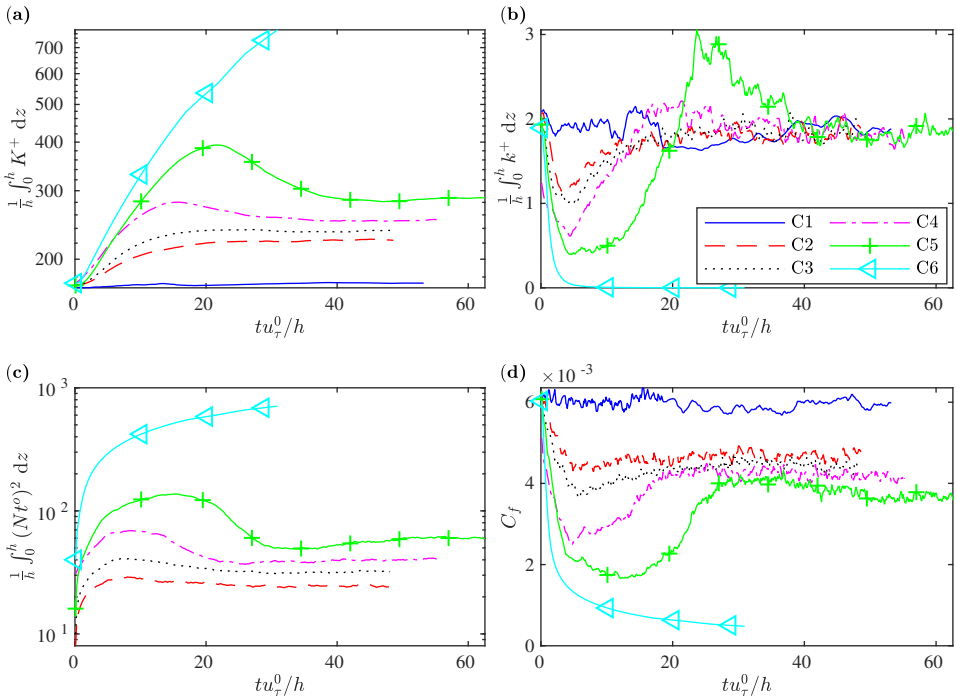

FIG. 1. Time series of (a) domain integrated MKE, (b) domain integrated TKE, (c) domain-integrated buoyancy frequency, and (d) friction coefficient for C1-C6.

are introduced.

It is worth discussing some of the differences between cases C1-C5 and those in Donda *et. al* [22, 23]. For C1-C5 there is no heat flux from the upper boundary and the lower boundary is continuously cooled. Thus the maximum sustainable heat flux (MSHF) [22], which is an upper limit for effective heat transfer across the channel height to balance wall cooling, is zero in C1-C5. In Donda *et. al* [22, 23] it is hypothesized that a stably stratified wall-bounded flow with heat entrainment from the upper boundary has a non-zero MSHF beyond which turbulence collapses. As mentioned earlier, turbulence recovers from partial collapse in C5 [4]. Interestingly, turbulence recovers for other more strongly stratified cases with $Ri_\tau \lesssim 2000$, $h/L_{MO} < 1.4$ if properly initialized but not for $h/L_{MO} \gtrsim 1.5$ (not shown here). For example, if a simulation with $Ri_\tau = 2000$ is initialized using $Ri_\tau = 1680$ simulation outputs at quasi-stationarity plus uniformly distributed random noise in velocity field with zero mean and variance of 0.2 turbulence recovers and acquires quasi-stationarity state. The initialization technique for a case with $Ri_\tau = 1680$ has been introduced at Sec. III A. Therefore, in C2-C5, the flow is limited by a minimum shear capacity (MSC) as discussed in van Hooijdonk *et. al* [30] (and not a MSHF), below which turbulence production cannot be maintained and starts to collapse. This difference suggests investigating turbulence collapse based on shear production as a more reliable approach.

Moreover, compared to the work of Taylor and coworkers (Fig. 8 in Taylor *et. al* [16] and Fig. 3 here), after reaching quasi-stationarity the velocity fluctuations in the inner layer are not significantly sensitive to the location of the imposed stable stratification. Similar results are obtained whether it is imposed at the bottom wall where turbulence is being generated,

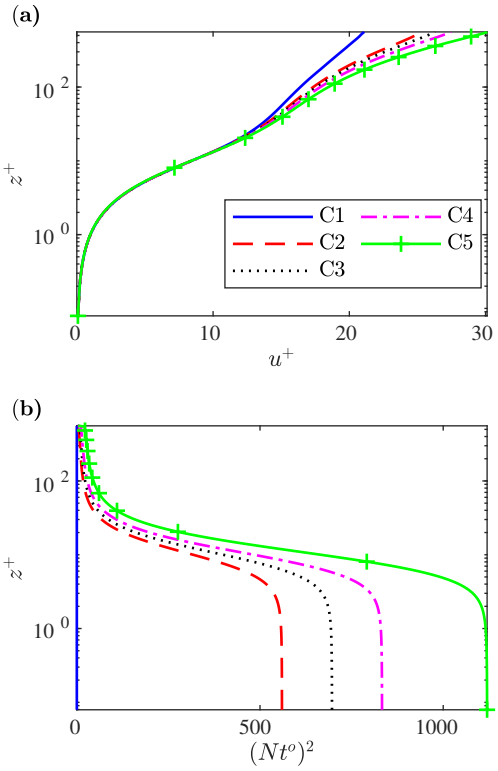

FIG. 2. Horizontally averaged profiles of (a) streamwise velocity and (b) buoyancy frequency.

or at the upper boundary where there is no source of turbulence production. This similarity among velocity statistics regardless of the choice where stable stratification introduced is due to the fact that shear dominates over buoyancy in the quasi-stationary state, as will be shown in Sec. III C.

Profiles of mean and root-mean-square (RMS) temperature are shown in Fig. 5. It is clear that increasing Ri_τ results in stronger temperature gradient and N^2. Temperature fluctuations are relatively small everywhere, with somewhat higher values as Ri_τ increases. The effect of Ri_τ become more clear in the outer layer as shown in Fig. 5b where wall-generated shear becomes less dominant.

The tangential Reynolds stress is shown Fig. 6(a). Stratification leads to a monotonic decrease of $-\overline{u'w'}$ at all heights. This decrease in $-\overline{u'w'}$ with increasing Ri_τ explains the flow acceleration by stratification in Fig. 2a. Turbulent heat fluxes are shown in Fig. 6(b-c). The streamwise turbulent heat flux is an order of magnitude larger than the vertical heat flux. The larger values of streamwise turbulent heat flux are due to the fact that streamwise velocity fluctuations are largest compared to the wall-normal and spanwise counterparts. Profiles of $\overline{u'\theta'}$ and $-\overline{w'\theta'}$ closely follow the profiles of $\overline{u'^2}$ and $\overline{w'^2}$ in Fig. 3(a,c) by a factor of $O(10^{-3})$ signifying small values for θ' correlating with u' and w'. Additionally, Fig. 3(a,c) and Fig. 6(b,c) together show that the normalized correlation between fluctuating streamwise velocity and temperature $R_{u\theta} = \overline{u'\theta'}/(\sqrt{\overline{u'^2}}\sqrt{\overline{\theta'^2}})$ is larger than the normalized correlation between fluctuating wall-normal velocity and temperature $R_{w\theta} = \overline{-w'\theta'}/(\sqrt{\overline{w'^2}}\sqrt{\overline{\theta'^2}})$. The larger normalized correlation between u' and θ' suggests that the effect of buoyancy is more pronounced in the evolution of the quantities that directly depend on $\overline{u'\theta'}$ (e.g. evolution of turbulence production as in tangential Reynolds stress budget equation) rather than $\overline{w'\theta'}$ (e.g. evolution of the variance of vertical velocity fluctuations).

C. Buoyancy Reynolds number and gradient and flux Richardson numbers

In this section, we aim to further explore the nature of stable stratification caused by wall cooling in C2-C5. To do so, we relate stratification effects to the mean shear and turbulence dissipation, which control the characteristics of the turbulence and thus momentum mixing. To reach this goal we use three different non-dimensional parameters by which stratification can be quantified: the buoyancy Reynolds number Re_b, gradient Richardson number (Ri_g) and flux Richardson number (Ri_f).

The buoyancy Reynolds number is defined as [31]

$$Re_b = Re_\tau \frac{\epsilon}{N^2}, \tag{7}$$

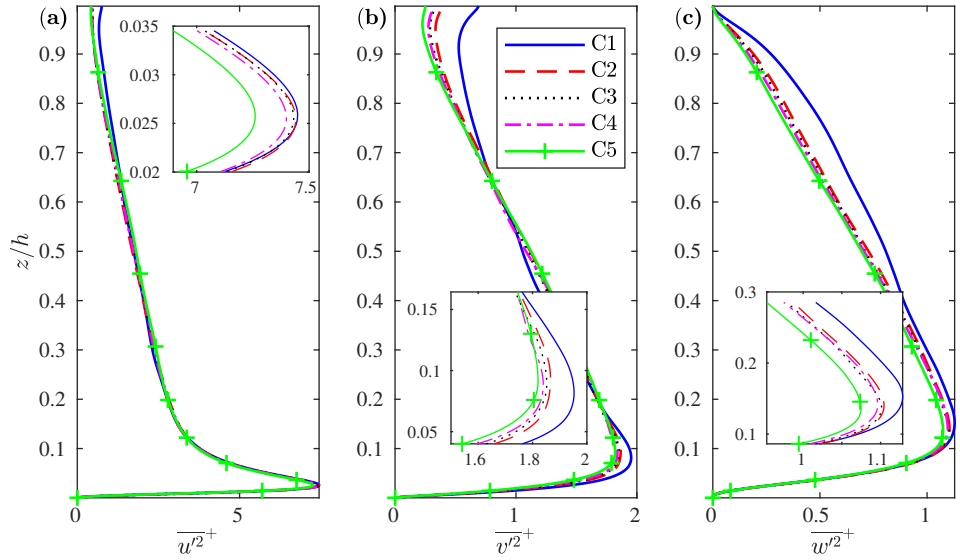

FIG. 3. Second order moment of fluctuations of (a) streamwise velocity ($\overline{u'^2}$), (b) spanwise velocity ($\overline{v'^2}$), and (c) vertical velocity ($\overline{w'^2}$).

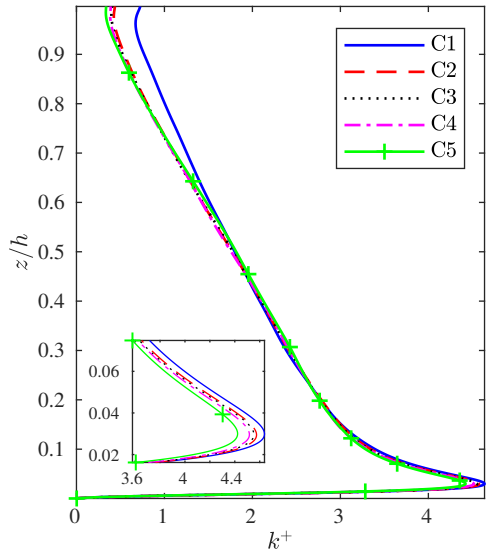

FIG. 4. Turbulent kinetic energy profile.

where horizontally and temporally averaged values are used for the kinetic energy dissipation ϵ and buoyancy frequency. Re_b is related to the ratio of the Ozmidov to Kolmogorov scales (both will be defined in Sec. III G), and quantifies the range of small scales that are not affected by stratification [32, 33]. Regions with $Re_b \gg 1$ include overturning, enhanced mixing, and more isotropic small-scale turbulence. Vertical profiles of Re_b are shown in Fig. 7(a). Even in C5, the minimum value of $Re_b \gtrsim 50$ for $z/h \leq 0.8$, showing that there are inertial range eddies that are not significantly affected by stratification [33], similar to a weakly stratified case. Therefore, features of near-wall turbulence are far from the viscously coupled stratified turbulence (VCST) regime with $Re_b < 1$ [4, 34, 35]. By contrast, at early times in C5, during the decay and early stages of the recovery phase, VCST was the dominant feature of the near-wall region, which had $Re_b < 1$ [4].

The gradient Richardson number is defined as [9, 36]

$$Ri_g = \frac{N^2}{S^2}, \tag{8}$$

where $S = \partial\overline{u}/\partial z$. The gradient Richardson

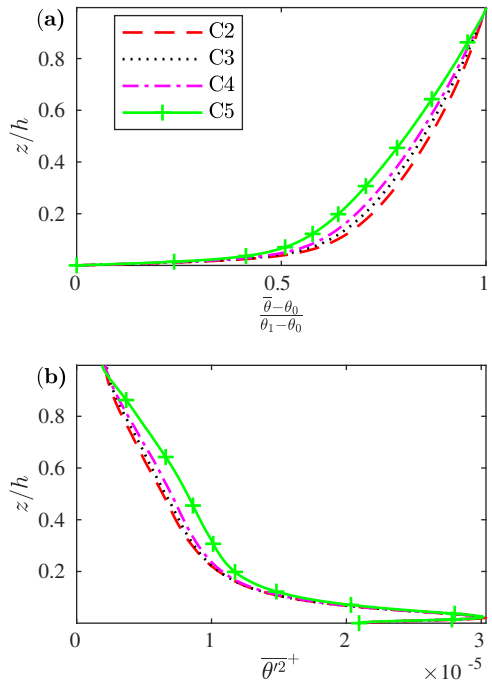

FIG. 5. First and second order statistics for temperature field. (a) mean, and (b) root-mean-square. The θ_0 and θ_1 in (a) are values of mean temperature at bottom ($z/h = 0$) and top boundary ($z/h = 1$), respectively.

number shows regions of the flow where either buoyancy or shear dominates. In shear-dominated regions, turbulence is enhanced and mixing becomes stronger. Only the regions above $z \approx 0.9$ satisfy the criteria $Ri_g > 0.25$ [36] and mean shear dominates everywhere else for all cases, as shown in Fig. 7(b). Therefore, it is expected that near-wall turbulence in the stratified cases is similar in C2-C5 since Ri_g is relatively small for all stratifications. The small values for Ri_g near the wall are due to the fact that mean shear near the wall is very large and almost independent of stratification (Fig. 2a) in the quasi-stationary state. Therefore, Ri_g becomes very small near the wall $z < 0.1$ with only a small dependence on stratification.

The flux Richardson number is defined as [16]

$$Ri_f = \frac{-B}{-B+\epsilon}, \tag{9}$$

where horizontally and temporally averaged values are used for the viscous dissipation (ϵ) and buoyancy destruction (B) (these quantities will be defined and described in more detail below). Effectively Ri_f is the ratio between buoyancy destruction B and TKE production P, where the balance $P \sim -B - \epsilon$ is used to have meaningful values where P is small within the logarithmic and outer layer regions. Therefore Ri_f measures the work that is needed to overcome the destroying effect of stable stratification that may lead to reduction in momentum mixing [16]. The Ri_f in Fig. 7(c) increases with increasing stratification at all heights. Also, Ri_f increases when moving away from the wall until $z \approx 0.8$. Therefore, with increasing height, more work is needed to overcome the destroying effect of buoyancy until $z \lesssim 0.8$, showing that the outer layer is mostly affected by stratification. Mean shear production dominates buoyancy in the near-wall region and the effects of stable stratification become minimal where $z \lesssim 0.2$. Above $z \approx 0.8$, Ri_f becomes smaller due to the impermeable free-slip-wall at the upper boundary.

Now let us return to the discussion of strong stable stratification prior to quasi-stationarity. To complement our qualitative observation of collapse and recovery at early times [4] we now quantify strong stable stratification with the gradient Richardson number, which gives a local measure of stratification strength. Profiles of Ri_g at different times in the inner region are shown in (Fig. 8). It is important to note that although the quasi-stationary value of Ri_g in the inner layer ($z \lesssim 0.2$) are less than 0.1 for C2-C5 (Fig. 7b), Ri_g acquires higher values in this region at earlier times of surface cooling process (Fig. 8). The values of Ri_g (Fig. 8d) in the inner region for C5 reaches 0.2, which is close to the threshold of 0.25 [37, 38] for the stability of stratified shear flow. This is in agreement with the appearance of intermittency in this re-

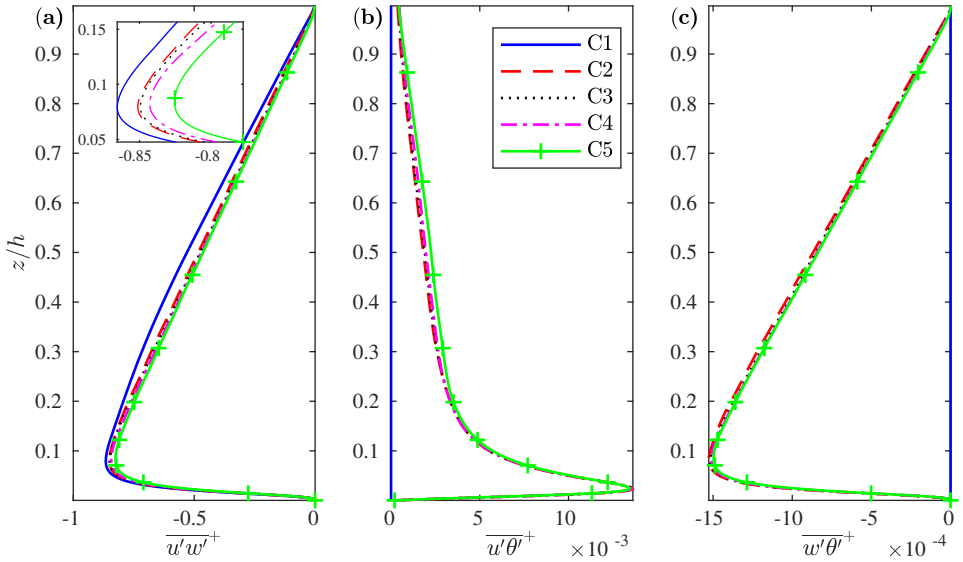

FIG. 6. Second order moment of (a) streamwise-vertical velocity fluctuations, (b) streamwise velocity-temperature fluctuations, (c) vertical velocity-temperature fluctuations.

gion at early times. In C6, Ri_g reaches 0.25 at early times (Fig. 8e) and turbulence in the near-wall region completely collapses (Fig. 1). The inner-region collapse of turbulence leads to full collapse of outer layer turbulence at subsequent times.

Due to the fact that turbulence in C6 fully collapses, leading to completely different boundary layer structures (e.g layered vortices as shown in Atoufi *et. al* [4]), quasi-stationarity is not reached for this case. Thus for the moderate Reynolds number considered here, the strongest surface cooling rate (set by Ri_τ) which may be imposed on a neutral open-channel flow while allowing for the recovery of fully developed turbulence must be between C5 and C6, i.e. Re_τ between 1120 and 2800. The relatively high values for Ri_g in the inner region in C5 confirms presence of strong stable stratification in this case earlier in the cooling process.

D. TKE budget

In this section, we aim to investigate the mechanisms that contribute to the TKE budget for quasi-stationary stably-stratified wall-bounded turbulence. The different terms in the TKE budget are defined in Appendix A and shown in Fig. 9: production P, dissipation ϵ, buoyancy destruction B, turbulent transport T, viscous diffusion D, and pressure work Π. It is noteworthy that buoyancy flux as sometimes used in the literature (e.g. Huang and Bou Zeid [12]) differs in sign from B. For clarity only cases C1, C3, and C5 are shown, and we focus on inner-layer balances where $z^+ \leq 100$. Although the major balance is between production and dissipation, stratification affects these two mechanisms only slightly. Overall, the behaviour is different from the transient case, where stratification has a significant impact on the evolution of TKE [4].

In general, the effects of stratification are more prominent going from the neutral case C1 to C2. For C2-C5, all of terms that contribute to the budget of TKE become close together

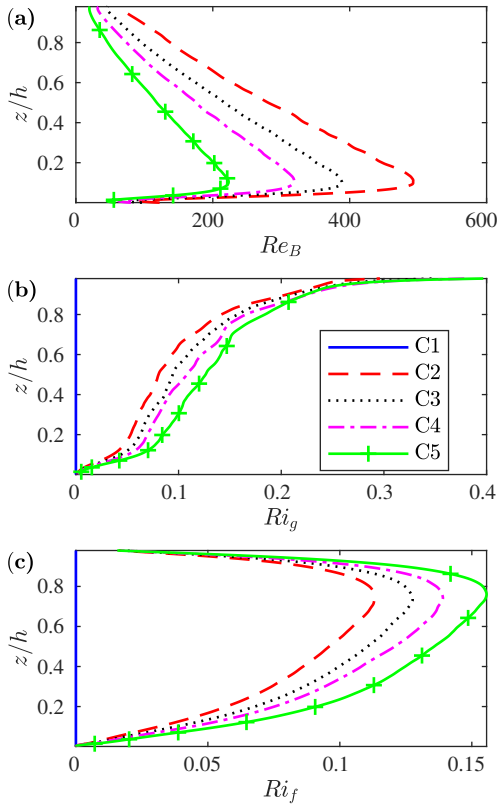

FIG. 7. Vertical profiles of (a) buoyancy Reynolds number, (b) gradient Richardson number, and (c) flux Richardson number.

even when Ri_τ increases by a factor of two from C2 to C5, which causes partial collapse before turbulence reaches stationarity [4]. Production and dissipation vary only slightly with stratification. Turbulence production in the inner layer decreases with increasing Ri_τ for $z^+ \gtrsim 20$ and increases with increasing Ri_τ for $z^+ \lesssim 20$. (Fig. 9a). Except in the viscous sublayer (VSL) where $z^+ \lesssim 5$, dissipation decreases with increasing Ri_τ. Stratification has a more significant effect on the smaller terms B, T, and Π. The buoyancy destruction B is an order of magnitude smaller than production and dissipation, which indicates that buoyancy destruction has a small impact on TKE exchange. The turbulent transport T is approximately equal to the transport of $\overline{u'^2}$ ($T \approx T_{11}$, see Appendix A). Interestingly, in the upper VSL, T decreases as Ri_τ increases. Its magnitude also decreases in the buffer layer as Ri_τ increases. As will be shown in Sec. III I, this change of T with stratification is consistent with weakening ejection and intensifying sweep events as Ri_τ increases.

The pressure-work term Π [39, 40] describes the work that is associated with the pressure field that can modify the kinetic energy of fluid elements. In the VSL, viscosity plays a significant role and the kinetic energy is not sufficient to initiate lift-up of the fluid elements. The pressure-work Π (along with D) can amplify kinetic energy of fluid elements to be sufficiently large for lift-up and escape from such a highly viscous region as the VSL. The largest values for Π are limited to the VSL, where Π decreases as Ri_τ increases. This decrease in Π with increasing stratification signifies that the ability of fluid elements to lift-up from the lower part of the VSL is reduced as Ri_τ increases.

In the VSL, viscous diffusion and pressure-work are energy sources. The net effect of these two TKE sources, along with dissipation, are transferred upward to the buffer layer by T. In the lowest part of the VSL $z^+ \leq 1$, where velocity fluctuations are small, D and ϵ balance each other. Thus, Π is the key mechanism in this part of the VSL to perform the work that is needed to transport fluid elements to the upper VSL where velocity fluctuations become stronger and T plays a more dominant role transferring TKE.

E. Inter-component energy redistribution

So far, we have explored the behaviour of the components of the velocity fluctuations and the TKE budget. An important question is how TKE is being distributed among horizontal and vertical components of velocity fluctuations. To analyze inter-component energy transfer at different vertical levels, the diagonal components of Φ_{ij} (Appendix A) are examined. These terms can be used because continuity implies that the pressure-strain mechanism does not contribute

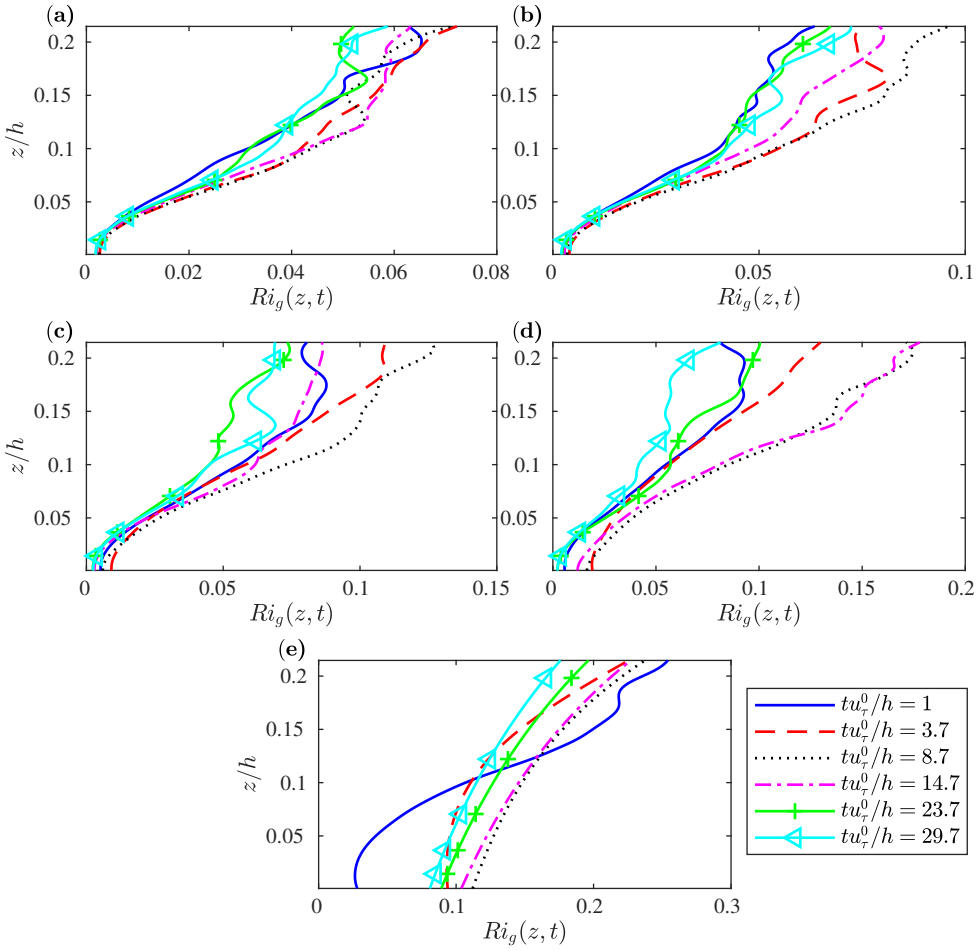

FIG. 8. Changes of gradient Richardson number over inner region at different times for (a) C2, (b) C3, (c) C4, (d) C5, and (e) C6. The u_τ^0 refers to friction velocity of neutral case. The outer layer part is not shown for clarity since Ri_g obtains large values in this region during the decay phase and early recovery phase of the cooling process.

to the budget of TKE and acts to redistribute among different portion of TKE.

Inter-component energy redistribution Φ_{ii} (no summation over i) is shown in Fig. 10. Overall, the dependence of the components of Φ_{ii} on z^+ is the same with stratification as without. In the lower part of the VSL $z^+ \lesssim 3$, Φ_{33} is a sink in the budget of $\overline{w'^2}$, and Φ_{11}, Φ_{22} are sources for $\overline{u'^2}$ and $\overline{v'^2}$ ($\Phi_{11}, \Phi_{33} > 0$). However, in that region Φ_{11} is small and TKE is transferred mostly from $\overline{w'^2}$ to $\overline{v'^2}$, showing that flow structures are becoming mostly lifted up. This flow of energy between fluctuating components may be due to vertical excitation of spanwise vortex rolls as in the early stage of hairpin vortex formation [41, 42]. In upper VSL ($3 \lesssim z^+ \lesssim 5$), TKE is extracted from $\overline{w'^2}$ and $\overline{u'^2}$ and distributed into $\overline{v'^2}$, which suggests lifting up of the legs of quasi-streamwise hairpin vortex [20, 21]. These vortical structures be-

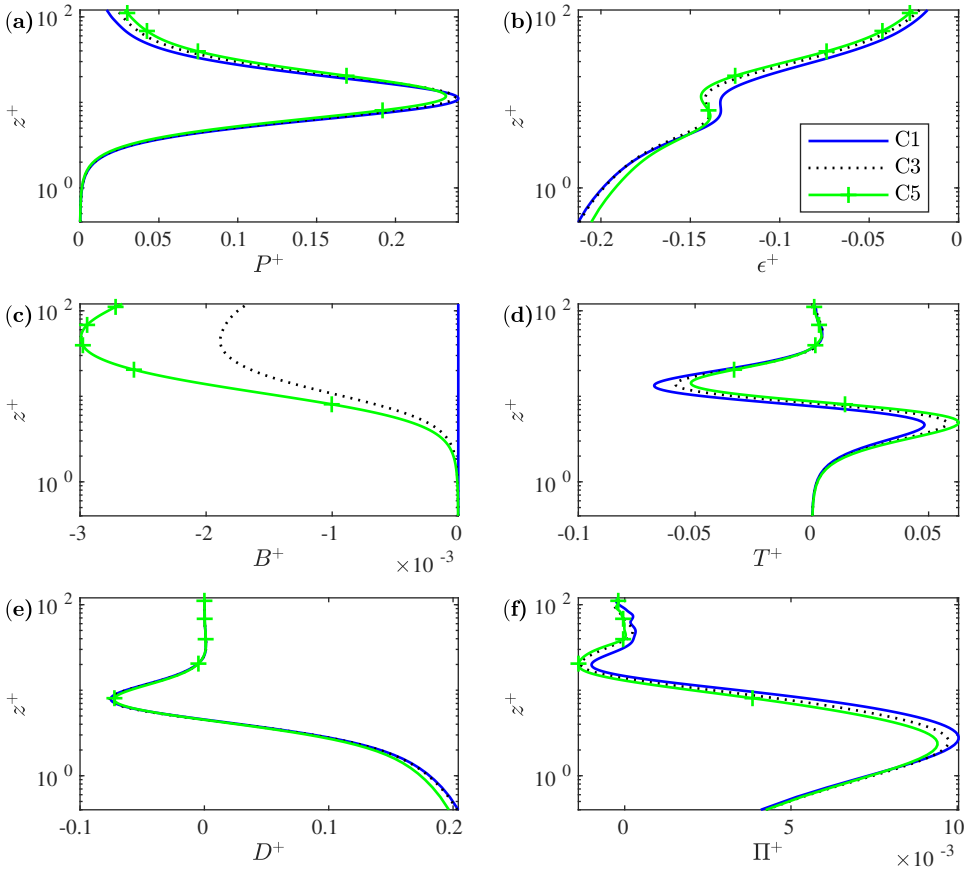

FIG. 9. Different contributions to the budget of TKE: (a) production, (b) dissipation, (c) buoyancy destruction, (d) turbulent transport, (e) pressure-work, and (f) viscous diffusion. Each term is scaled by Re_τ which is equivalent to conventional near-wall scaling by friction velocity u_τ and viscosity ν as ν/u_τ^2.

come more streamwise aligned moving upward into the buffer layer as Φ_{11} becomes increasingly negative while Φ_{22} and Φ_{33} become more positive.

In the lower buffer layer where $5 \lesssim z^+ \lesssim 10$, Φ_{11} becomes a considerable sink in the budget of $\overline{u'^2}$ showing that flow structures become dominantly streamwise aligned (e.g. formation of streaks from legs of hairpin vortices). TKE still redistributes from $\overline{u'^2}$ and $\overline{w'^2}$ to $\overline{v'^2}$, but the rate of energy distribution from $\overline{u'^2}$ intensifies compared to the upper VSL. From $z^+ \gtrsim 10$, TKE redistributes from $\overline{u'^2}$ to $\overline{v'^2}$ and $\overline{w'^2}$. Above the buffer region where $z^+ \gtrsim 30$, TKE is almost equally distributed from $\overline{u'^2}$ to $\overline{w'^2}$ and to $\overline{v'^2}$. In these inter-component TKE redistributions above the VSL, the magnitude of Φ_{11} and Φ_{33} increase as Ri_τ increases.

The change in Φ_{11} with stratification for $z^+ \gtrsim 10$ is more pronounced than that of Φ_{22} and Φ_{33}. This suggests stratification is in favor of straightening of tilted streamwise structures, as the decrease in Φ_{11} leads to decrease in Φ_{22} and Φ_{33}.

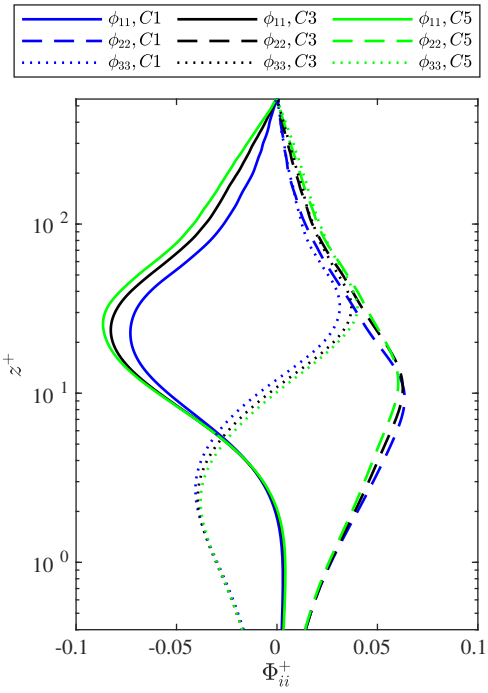

FIG. 10. Inter-component energy redistribution.

F. Budget of tangential Reynolds stress

In Sec. III D, we explored the budget of TKE at equilibrium. While production was influenced by stratification, the influence was less than expected. In this section, we aim to achieve a better understanding of why this is the case. To do so, we examine the budget of the tangential Reynolds stress, because of the key role that it plays in turbulence production.

The different contributions to the budget of $\overline{u'w'}$ are production (P_{13}), dissipation (ϵ_{13}), buoyancy destruction (B_{13}), turbulent transport (T_{13}), viscous diffusion (T_{13}), pressure-transport Π_{13}, and pressure-strain (Φ_{13}); these terms are defined in Appendix A and profiles are shown in Fig. 11. Similar to the TKE budget, we focus on inner layer balances. Interestingly for $\overline{u'w'}$, production P_{13} (Fig. 11a) and the buoyancy term B_{13} (Fig. 11c) are the same order of magnitude, showing that stratification has a more important effect on the budget of $\overline{u'w'}$ than the TKE budget. The maximum of P_{13} is in the buffer layer and is an order of magnitude larger than the dissipation ϵ_{13}. Another significant contribution to the budget of $\overline{u'w'}$ within the buffer layer comes from Φ_{13}.

Transfer of $\overline{u'w'}$ in part of the buffer layer where $5 \lesssim z^+ \lesssim 20$ corresponds to a sign change in T_{13} (Fig. 11d), which shows a transfer of tangential Reynolds stress from the wall to the upper boundary layer (ejection) for $z^+ \lesssim 10$ and from the upper boundary layer toward the wall (sweep) for $10 \lesssim z^+ \lesssim 50$. In both the VSL and the buffer layer, T_{13} shows a significant decrease from C1 to C2. B_{13} increases with stratification while ϵ_{13} and D_{13} are not very sensitive to stratification. The effect of stratification on Π_{13} is largest in the VSL. Above the VSL, stratification does not significantly affect these mechanisms within the inner layer. The magnitude of Φ_{13} in the VSL is increased with increasing Ri_τ. Very close to the wall where $z^+ < 1$, Φ_{13} and Π_{13} balance each other and ϵ_{13} is balanced by D_{13}. The maximum of B_{13} occurs at $z^+ \approx 15$. The neighbourhood of this location is associated with suppression of ejection and sweeping of tangential Reynolds stress as shown in Fig. 11(d).

The importance of buoyancy on the budget of the tangential Reynolds stress highlights the significance of stratification on the evolution of turbulence producing eddies. Thus it is expected that turbulence collapses at early stages of strong surface cooling when the time scale of turbulence producing eddies is larger than the time scale of buoyancy destruction through boundary layer growth [4]. As a result, they cannot adjust accordingly and the boundary layer cannot accommodate a buffer region [8] with net positive production.

Although we mainly discuss the quasi-stationary state, the hierarchy of the different terms in the Reynolds stress budget is independent of whether the transient or quasi-stationary state is considered. Hence, another motivation for the examination of the budget of $\overline{u'w'}$ is to have a clearer understanding of the mechanisms that most significantly contribute to the transiently evolving turbulence-

producing eddies seen in an earlier study for the same configuration [4]. The significance of buoyancy on the evolution of turbulence production rather than buoyancy destruction of TKE has been found in other flow configurations. Recently, Shah and Bouzeid [43] showed that for an evolving Ekman boundary layer under stable stratification, turbulence decay is controlled by the decrease in TKE production and not buoyancy destruction.

G. Length scales

Although relevant length scales for homogeneous stratified turbulence [44] and unstratified wall-bounded shear flows [45] have been studied independently in numerous studies [20, 33], far fewer studies have looked at length scales for stratified wall-bounded shear flows [16]. In this section, we examine various length scales, and also check the basic requirement for the grid scales to be smaller than that of the smallest dissipative eddies. Meeting this requirement implies we are accurately resolving the interaction of scales at all levels. Vertical grid-spacing is denoted by Δz and is a function of height due to grid-stretching.

We begin by looking at the Kolmogorov length scale due to its fundamental importance as the typical length scale of small, dissipative eddies in a turbulent flow. The Kolmogorov length scale is defined as

$$\eta = (Re_\tau^3 \epsilon)^{-1/4}. \tag{10}$$

It has recently been suggested that the Kolmogorov scale is not necessarily the smallest dissipative scale, particularly in regions of the flow that contain strong velocity gradients [46]. Since dissipation is governed by velocity gradients, it is useful to define scales that are derived based on statistics of velocity derivatives. Fine-scale structures in the velocity field are defined as [47]

$$\lambda_i^{u_i} = \left(\frac{\overline{\left(\frac{\partial u_i'}{\partial x_i} \right)^2}}{\overline{\left(\frac{\partial^2 u_i'}{\partial x_i^2} \right)^2}} \right)^{1/2}, \tag{11}$$

where the summation convention is not used. With this definition, $\lambda_i^{u_i}$ is the scale of momentum-carrying structures that are fine enough to capture both dissipation and diffusion process (u_i-structures hereinafter). The consideration of diffusion becomes important in the lower VSL where viscous dissipation and diffusion have similar values. In particular for $w-$structures, wall impermeability imposes very small values for wall normal velocity in the lower VSL and having the correct turbulent diffusion becomes very important.

Shear generated by the presence of the wall plays a key role in maintaining turbulence production for wall-bounded turbulence. If l_C is the length scale of the eddies that have time scales comparable to mean shear S, then their velocity is of order $u_{l_C} \approx (\epsilon l_C)^{1/3}$ [45] using the inertial-range approximation. Therefore, from $l_C/u_{l_C} = 1/S$, the Corrsin length scale is defined as [45]

$$l_C = \left(\frac{\epsilon}{S^3} \right)^{1/2}. \tag{12}$$

The Corrsin scale is typically used in shear flows [45].

In stratified turbulent flows it is common to define a characteristic scale of stratification, which we will denote as l_O, for which there is a balance between inertial and buoyant effects [33]. This scale is called the Ozmidov scale and is defined as,

$$l_O = \left(\frac{\epsilon}{N^3} \right)^{1/2}. \tag{13}$$

Analogous to the Corrsin scale, l_O is the scale at which the eddy time scale is similar to N.

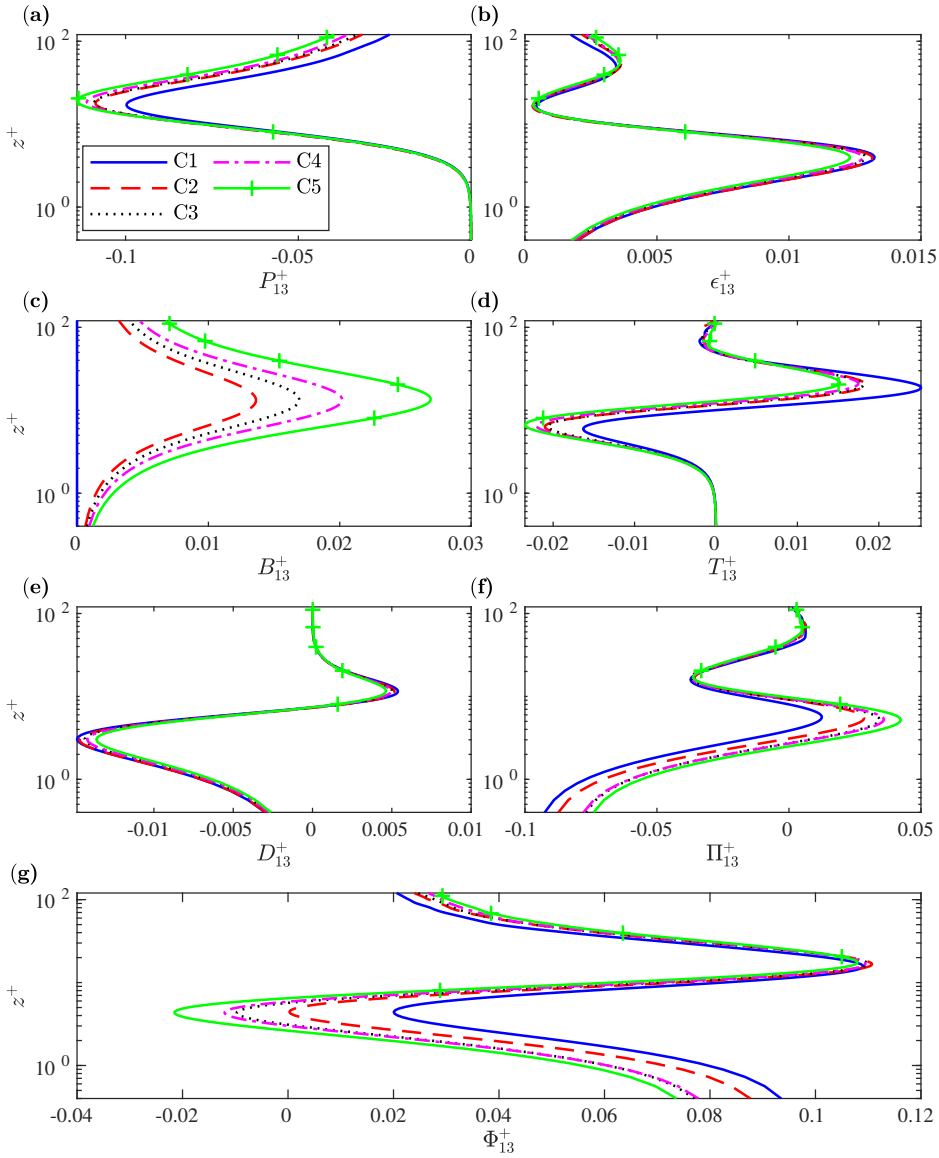

FIG. 11. Different contribution to the budget of $\overline{u'w'}$: (a) production, (b) dissipation, (c) buoyancy destruction, (d) transfer, (e) viscous diffusion (f) pressure transport, and (g) pressure-strain.

Therefore, stratification has a negligible effect on turbulence for scales much smaller than l_O, and the effect of stratification becomes dynamically important when the eddy size is similar to or greater than the Ozmidov scale.

All the length scales that have been discussed so far depend on velocity fluctuations and are therefore inherently linked to the kinetic energy of the flow. It is also important to identify scales that primarily involve potential energy. The Ellison scale l_E is a distance that a fluid particle can travel before all of its kinetic energy trans-

fers to potential energy and transfer back toward equilibrium position [48, 49]. Therefore, the Ellison scale is an overturning scale and it is defined as [16, 48–50]

$$l_E = \frac{\sqrt{\overline{\theta'^2}}}{\overline{\frac{\partial \overline{\theta}}{\partial z}}}. \tag{14}$$

Figure 12 shows these length scales as functions of height from the wall. In Fig 12(a) we can see first of all that η and l_C are smaller than the Ozmidov scale. The Kolmogorov scale shows little dependence on stratification, while the Corrsin scale does show some dependence on stratification in the outer region above $z^+ \approx 100$, where l_C decreases as Ri_τ increases. This is particularly interesting because they are still smaller than the Ozmidov scale. Note also that the Corrsin scale is smaller than the Kolmogorov scale below $z^+ \approx 10$ in Fig 12(a), implying that all scales are affected by strong near-wall shear. Both the Kolmogorov and Corrsin scales are indeed larger than the grid scale, indicating that the flow is well resolved.

Fine scales of w-structures (λ_z^w), shown in Fig. 12(b), are smaller than η in the lower VSL where $z^+ \lesssim 1$ as a result of wall-impermeability leading to small vertical velocity. Moreover, the limiting behaviour of the velocity fluctuations [51, 52] leads to a linear profile for λ_z^w close to the wall [47]. The λ_x^u, λ_y^v, and λ_z^w fine scales of velocity structures are smaller than the Ozmidov scale and are not sensitive to stratification at all vertical levels, as shown in Fig 12(b). As expected, the outer layer values of λ_x^u, λ_y^v, and λ_z^w are similar, indicating that small scales in that region are close to isotropic. Fine structures of u are larger than the other components and fine structures of w are the smallest.

Fig. 12(c) shows the Ellison scale, which does not exhibit a dependence on Ri_τ in the near-wall region. However, l_E is sensitive to stratification in the outer layer, although it is smaller than l_O.

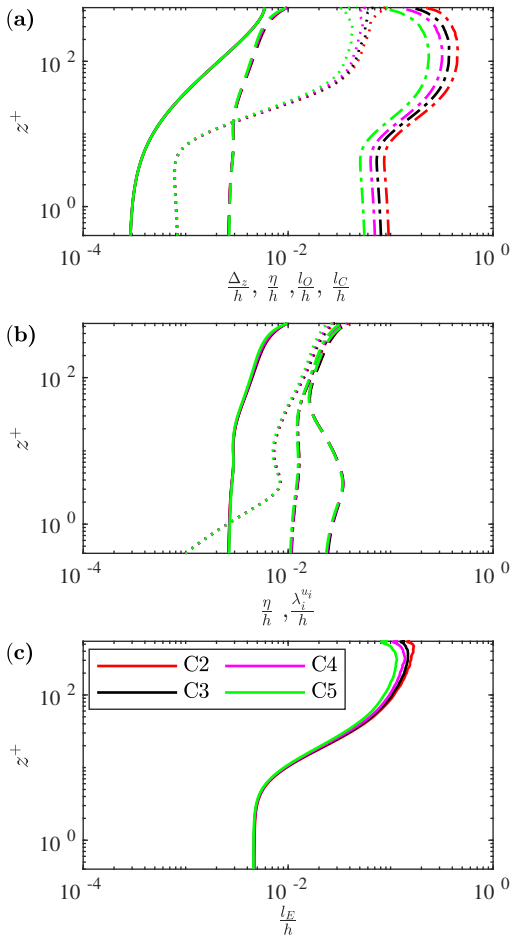

FIG. 12. Length scales as a function of wall normal distance. (a) grid (solid lines), Kolmogorov (dashed lines), Corrsin (dotted lines), and Ozmidov scales (dash-dotted lines). (b) Kolmogorov scales (solid lines), fine scales of w-structures (dotted lines), v-structures (dash-dotted lines), and u-structures (dashed lines). (c) Ellison scales.

H. Kinetic energy spectra and horizontal scales

To address vertical dependence of the horizontal length scales that may contribute to the kinetic energy cascade we look at premultiplied streamwise and spanwise energy spectra as a function of height. The pre-multiplied energy

spectra are defined as

$$\phi_E^x(k_x, z) = \frac{k_x}{2} \sum_{k_y} k_y \widehat{u}_i \widehat{u}_i^*, \tag{15}$$

$$\phi_E^y(k_y, z) = \frac{k_y}{2} \sum_{k_x} k_x \widehat{u}_i \widehat{u}_i^*, \tag{16}$$

where $\widehat{(\,)}$ refers to Fourier transform, $*$ represents complex conjugate and k_x and k_y are wavenumbers in streamwise and spanwise directions. Premultipied spectra are frequently shown [9, 53, 54] because of their relationship with kinetic energy. For example, spanwise averaged kinetic energy corresponds to $\int E \, \mathrm{d}k_x = \int \phi_E^x \, \mathrm{d}(\log k_x) = \int \phi_E^x \mathrm{d}(\log \lambda_x)$ where $E = \sum_{k_y} \widehat{u}_i \widehat{u}_i^*/2$ and $\lambda_x = 2\pi/k_x$ is the wavelength in the streamwise direction. A similar expression is valid for the streamwise averaged kinetic energy. Thus, on a logarithmic wavelength axis, ϕ_E^x and ϕ_E^y visualize spectral energy densities [9] for streamwise and spanwise wavelengths, respectively.

The premultiplied spectra are shown in Fig 13. For clarity, only spectra for cases C1 and C5 are shown. It can be seen that the energetic scales in the buffer layer in the spanwise direction are smaller than those in the buffer layer in the streamwise direction. For example, the contours containing 90% of the spectral energy density are centered at $\lambda_y \approx 100$ and $\lambda_x \approx 800$ for spanwise and streamwise scales, respectively. The λ_x and λ_y corresponding to each contour line at all levels become slightly smaller with increasing stratification. The inclination of spectral energy density contours with height (dashed-dotted line in Fig 13(a)) for the spanwise scales is more pronounced in comparison to the streamwise scales (Fig 13(b)). This difference suggests that widening of spanwise scales with respect to height occurs at a larger rate compared to elongating of streamwise scales. Large outer-layer spanwise scales with $\lambda_y \gtrsim L_y$ ($\lambda_y^+ \gtrsim 1760$) contain only $\lesssim 10\%$ of spectral energy density as shown in Fig 13(a). However, they penetrate down to VSL. Large outer-layer streamwise scales with $\lambda_x \gtrsim L_x$ contain $\gtrsim 40\%$ of the spectral energy density, as shown in Fig 13(b). However, they do not contribute significantly to statistics as shown below, probably due to the paucity of those scales [55]. Large outer-layer streamwise structures of the size $\lambda_x \gtrsim L_x$ ($\lambda_y^+ \gtrsim 3520$) contain $\lesssim 10\%$ of the spectral energy density and have also their roots in the VSL.

For the neutral case, spanwise length scales increase monotonically with height and contour lines of spectral energy density show a relatively symmetric shape around the reference line $\lambda_y \propto z$. Interestingly, for strongly stable stratification, this symmetry of the spectral energy density around the line $\lambda_y \propto z$ is broken for spanwise scales (in Fig. 13a) while the shape of spectral energy density for streamwise scales is approximately preserved (Fig. 13b). Thus, distribution of kinetic energy among different λ_x scales does not change significantly with stratification at all heights. In C5, the change of λ_y with height that contribute between 30% and 70% of the ϕ_E^y is smaller in comparison to the scales that contribute more than 70% of ϕ_E^y. For scales that contain less than 30% of ϕ_E^y in C5, the increase with height is smaller compared to scales that contain a similar portion of ϕ_E^y in C1. Thus, stratification causes asymmetry in distribution of kinetic energy among different λ_y scales with respect to height.

I. Higher-order statistics

Higher-order statistics can provide additional insight into our understanding of the distribution of TKE. For example, third-order moments of velocity fluctuations can provide insight into energy transfer and fourth-order moments can accentuate activities of less energetic scales. We scale $\overline{u'^2}$ and $\overline{u'^4}$ by their maximum so that both have values between zero and one. Then, below the log-region where the flow is energetic these profiles look similar. However, above that region where the flow is less energetic, the difference between these scaled profiles become more prominent (not shown).

Plots of $\overline{u'^3}$ with respect $\overline{u'^2}$ and $\overline{u'^4}$ are presented in Fig. 14. Third order moments of u'

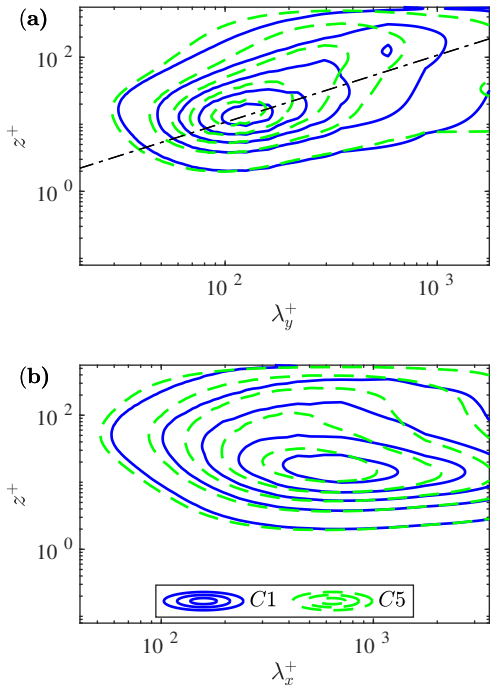

FIG. 13. Spectral energy density (a) ϕ_E^y and (b) ϕ_E^x. Blue and green lines correspond to C1 and C5 respectively. Contours are plotted at the level of 0.1, 0.3, 0.5, 0.7, and 0.9 of maximum values of the corresponding spectrum. The slope of the black diagonal dash-dotted line is 1 in (a) where $z = \dfrac{60}{Re_\tau}\lambda_y$.

and w' are correlated with the transfer of $\overline{u'^2}$ and $\overline{w'^2}$ (T_{ij} term in Appendix A). By comparing Fig. 14(c,d) one can say is that $\overline{u'^2}$ and $\overline{u'^4}$ are strongly correlated (a similar relationship is seen for $\overline{w'^2}$ and $\overline{w'^4}$). Similar results have been found in LES simulations of atmospheric boundary layers [56]. From the modeling perspective, this strong correlation between second and fourth order statistics suggest that a linear model that relates fourth order moments and second order moments can be used to represent effect of fourth order moments. This results supports quasi-normal approximation [56–58] which can be used in model development [58, 59].

Also, strong positive fluctuations in $\overline{u'^3}$ are enhanced as stratification increases, while strong negative ones are weakened. Therefore, stratification is in favor (in a quasi-stationary sense) of intensifying high-speed streaks and weakening low-speed streaks (Fig. 14a). Positive streamwise velocity fluctuations can be seen (Fig. 15) to increase in the upper VSL as Ri_τ increases whereas negative streamwise velocity fluctuations in the buffer layer decrease. For $\overline{w'^3}$, the positive vertical velocity fluctuations are strongly weakened and the magnitude of the negative vertical velocity fluctuations are slightly increased, in particular in the log region.

This behaviour of third-order velocity statistics can be summarized in terms of a Q2 (ejection) and Q4 (sweep) map. As shown in Fig. 15c, ejection events (Q2) are hindered as Ri_τ increases and sweeping events (Q4) are less affected compared to the neutral case, consistent with earlier studies [13, 16]. The larger effect of stratification on ejection events is due to the fact that these events are strongest close to the wall where N^2 is largest. Therefore, buoyancy restoring force has more effect on these events rather than sweeping events, which are initiated further from the wall with a smaller N^2 [13, 16].

J. Effect of heat entrainment from upper boundary

For the stratified cases shown so far (C2-C5), we have neglected the effect of possible heat transfer from the upper boundary. In doing so, we have isolated near-wall turbulence from modulations caused by stable stratification (i.e. capping inversion) due to heat entrainment at the upper boundary. As discussed by Atoufi *et. al* [4], heat entrainment from the upper boundary results in weakening of the outer layer eddies, which can significantly affect the wall turbulence. These outer layer eddies play an important role in turbulence recovery for strong stable stratification. Removing them from the flow results in full collapse of turbulence dur-

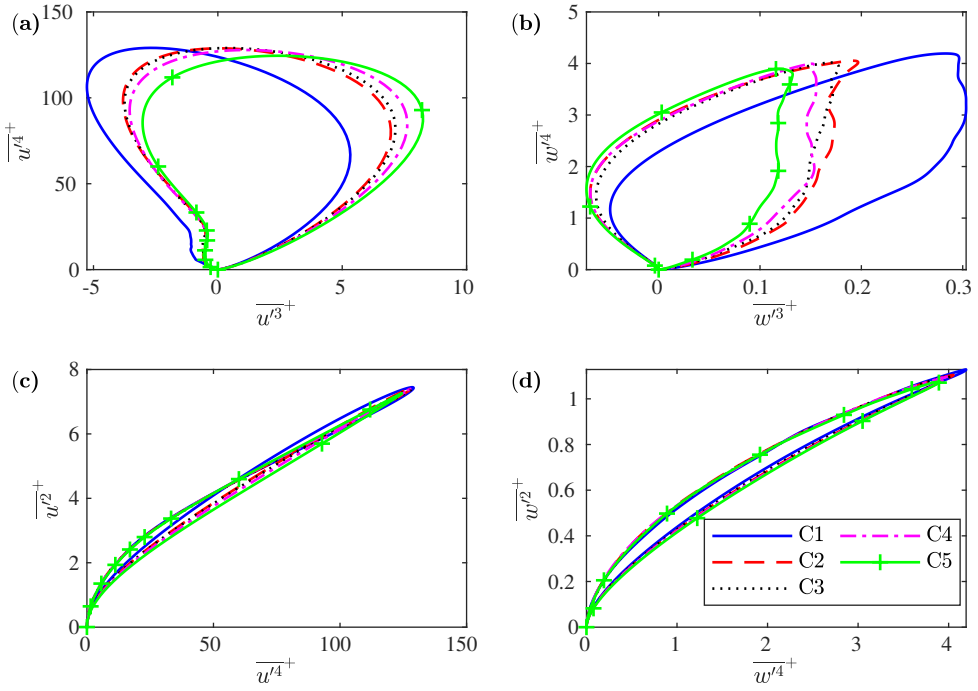

FIG. 14. Profiles of (a) third-order versus fourth-order moments of streamwise velocity fluctuations, (b) third-order versus fourth-order moments of vertical velocity fluctuations, (c) fourth-order versus second-order moments of streamwise velocity fluctuations, and (d) fourth-order versus second-order moments of vertical velocity fluctuations.

ing transient cooling [4], and intensifying their available TKE, even by 10%, can enable recovery from collapse [8].

In this section, we study the effect of the upper thermal boundary condition on statistics of the quasi-stationary state. To do so, we compare C2 and C5 with C2D and C5D. In C2 and C5 heat transfer from the upper boundary is not permitted. Cases C2D and C5D use Dirichlet upper boundary conditions and therefore allow entrainment of heat from the upper boundary. For C2D and C5D, simulations are initialized using fields from the quasi-stationary states from C2 and C5, respectively. As shown in Fig. 16(a) heat entrainment from the upper boundary results in trends for TKE that are similar to more weakly stratified cases (see Fig. 1b) when stratification is imposed only at the bottom wall such as C2 (see Atoufi *et. al* [4] for the temporal evolution of C2-C5). In both C2D and C5D, turbulence first undergoes a decay until $t \approx 5$ and then starts recovering afterward. However, the overshoot of domain integrated TKE in C5 is not observed for C5D. An important point here is that turbulence can recover from initial decay with or without entrainment of heat from the upper boundary. To distinguish between these two situations, one can say that the former flow is limited to a maximum sustainable heat flux [22, 23] and the latter flow is limited to a minimum shear capacity to sustain turbulence [30] (see Sec. III B for more detailed explanation).

The profile of TKE in Fig. 16(b) shows that the upper thermal boundary condition can modulate flow characteristics (e.g. TKE, mean shear, and N^2) for $z \gtrsim 0.3$ in the quasi-stationary state. Compared to C5, C5D has

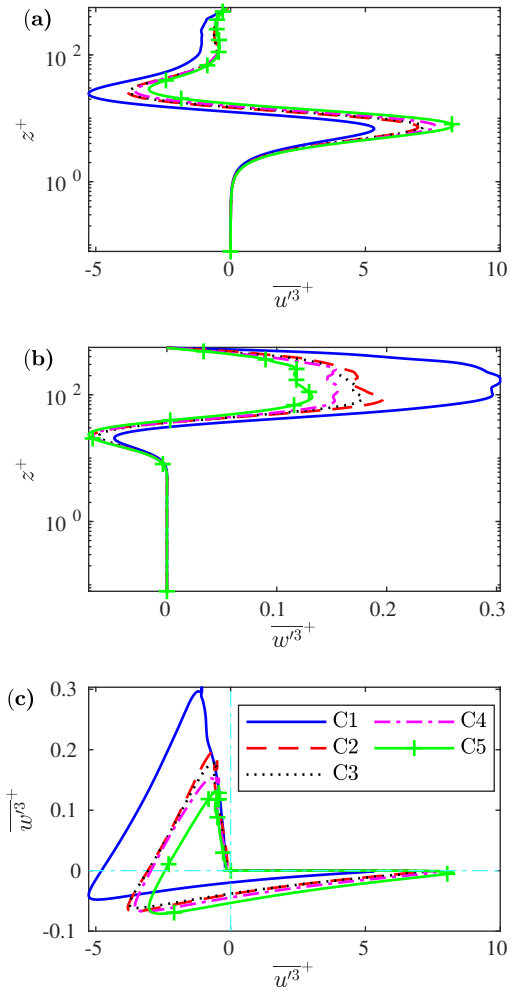

FIG. 15. Vertical profile of (a) third-order moment of streamwise velocity fluctuations and (b) third-order moment of vertical velocity fluctuations, and (c) $\overline{w'^3}$ versus $\overline{u'^3}$ for analysis of quadrant events (Q1-Q4).

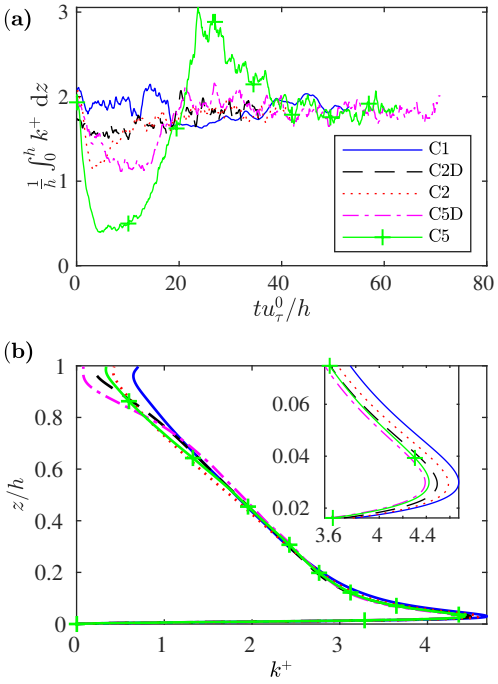

FIG. 16. Effects of heat entrainment from the upper boundary on (a) domain-integrated TKE and (b) vertical profile of TKE.

lower TKE for $z > 0.8$. Moreover, in C5D the flow acceleration due to reduced tangential Reynolds stress leads to larger streamwise velocity for $z > 0.3$ (Fig. 17a). The temporal evolution of domain integrated TKE suggests that entrainment of heat from the upper boundary also has a transient effect and if turbulence approaches quasi-stationary state the TKE become close to the weakly stratified case. A strong capping inversion caused by heat entrainment from the upper boundary can be clearly seen in Fig. 17b, where for $z > 0.3$ buoyancy restoring force significantly increases. The effect of heat entrainment from the upper boundary is significant on mean flow velocity and buoyancy frequency above the buffer layer. However, TKE for all stratified cases shows similar behaviour (Fig. 16b and also Fig. 19 in Taylor *et. al* [16]). This similarity strongly suggests that characteristics of stably-stratified wall-turbulence become similar to weakly stratified cases if quasi-stationarity is acquired. This similarity means that, regardless of the choice of the upper boundary condition, the TKE profile becomes roughly similar to weakly stratified cases.

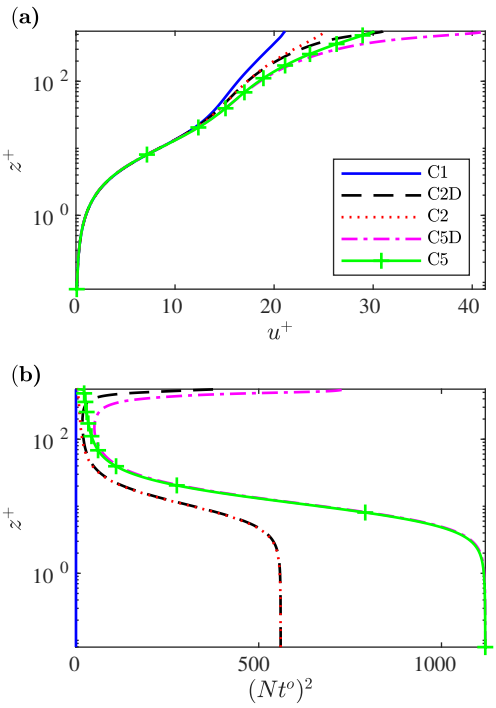

FIG. 17. Effects of heat entrainment from upper boundary on (a) mean velocity profile and (b) buoyancy frequency.

K. Computational domain size effect

Results presented so far were obtained on a domain of medium size [53, 60] with $L_x = 2\pi$ and $L_y = \pi$. For the unstratified case, such a domain contains a few minimal flow units [61] including at least one ejection and one sweep [62]. Here we examine the effect of the computational domain on mean flow behaviour, second-order statistics, and energy spectra. In this section the results from a larger domain simulation L5D with $L_x = 8\pi$ and $L_y = 6\pi$ are compared to medium domain case C5DC, which both have the same grid resolution, which is lower than that of the main simulations C1-C5. Note that these simulations employ Dirichlet boundary conditions at the upper boundary and therefore have heat entrainment. The size of the larger domain was chosen based on the study of García-Villalba and del Álamo [9].

The mean flow velocity and temperature profiles for medium and large domain size simulations in Fig. 18 look quite similar. This is consistent with unstratified channel flow simulations [60]. The only slight differences between medium and large domains are observed for $z > 0.6$. Second-order statistics of velocity and temperature also have similar profiles for medium and large domain sizes, as seen in Fig. 19. The turbulent heat flux in the vertical direction shows slightly larger sensitivity to the choice of domain size.

The streamwise-averaged pre-multiplied kinetic energy spectrum for the smaller domain shows that it is already sufficient to represent the scales in the spanwise direction (Fig. 20a). The widest structures belong to the outer layer whereas the tallest structures are streaks that belong to the buffer layer, where $10 \lesssim z^+ \lesssim 20$. Streaks with size $\lambda_x \leq L_x$ in the buffer layer contain $\gtrsim 60\%$ of energy spectrum as shown in Fig. 20(b). As expected, spanwise length scales are typically smaller than streamwise length scales. Moreover, and consistent with earlier studies [55], the spectrum for the small domain closely follows that for the larger domain up to the cutoff wavelength that is set by the domain size in the streamwise direction. It is worth mentioning that the tall length scales in Fig. 20(b), with $\lambda_x \approx 25h$ and about 10% of the TKE, are likely attached inactive structures [63]. These structures enhance viscous dissipation as they are connected to the VSL [64]. These inactive structures most likely contain swirling or meandering type of motions [63] which will not contribute to top-down transferring of tangential Reynolds stresses.

IV. CONCLUSION

In this paper, near-wall turbulence under strong stable stratification has been studied using DNS. To address the effects of stable stratification on the characteristics of near-wall turbulence, five different high-resolution cases (C1-C5) are considered with different Richardson

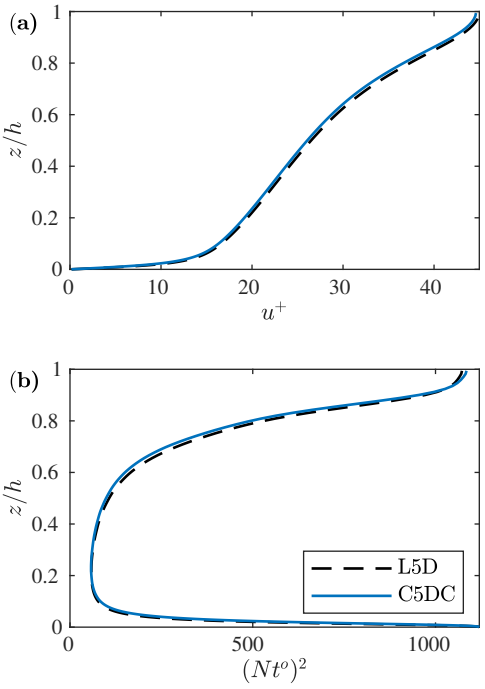

FIG. 18. Computational domain size effect on (a) mean velocity profiles and (b) buoyancy frequency.

numbers ranging from the neutral to strongly stable stratified regime.

The configuration for cases C1-C5 was chosen similar to Atoufi *et. al* [4] to analyze the response in the near-wall region due to stratification imposed by bottom wall cooling. Although this response was found to be significant in the transient case [4], at quasi-stationarity the impact is much smaller. Nonetheless, in the near-wall region, where $z \lesssim 0.1$, stratification leads to a decrease in velocity variances, TKE, tangential Reynolds stress, and heat flux in the streamwise and wall-normal direction. Using analysis of higher-order statistics it was shown that the tendency of streamwise velocity fluctuations to acquire positive values is intensified as stratification increases.

Mean flow velocity above $z^+ \gtrsim 10$ is increased as Ri_τ increases due to flow acceleration caused by a reduction in near-wall tangential Reynolds stress. The buoyancy restoring force is strongest at the wall and becomes weaker moving away from the wall. Increasing Ri_τ intensifies this restoring force. However, the shear stress generated by the mean shear dominates these buoyancy forces. By analyzing Re_b it was shown that for C2-C5, overturning and not layering of vortical structures is a dominant feature of eddy motions in the near-wall region if quasi-stationarity is reached. Up to $z \lesssim 0.8$, the flux Richardson number is reduced with increasing height and stratification.

Analysis of the TKE budget shows that production and dissipation are the dominant terms in balancing TKE above the VSL and buoyancy destruction does not significantly affect the TKE budget. It was shown that very near the wall where $z^+ \lesssim 1$, velocity fluctuations are small and pressure-work term plays an important role in transferring TKE to higher-momentum fluid farther away from the wall. To further explore the effects of stratification on turbulence production, we examined the budget of tangential Reynolds stress. By doing so, it was shown that buoyancy has a considerable effect on the budget of tangential Reynolds stress. Therefore, the appearance of patchy turbulence during the cooling process due to a lack of production (and not excessive dissipation [4]) is likely linked to the significance of buoyancy destruction on the evolution of tangential Reynolds stress.

By analyzing length scales, it was found that in the outer layer, $z^+ \gtrsim 100$, for each Ri_τ: $l_O > l_E > l_C$. Each of these scales shows some sensitivity to stratification. It was shown that there are scales smaller than the Kolmogorov scale that may be important for wall-bounded stratified turbulence. Particularly in the VSL, the Corrsin scales are smaller than Kolmogorov scales. Very near the wall where $z^+ \gtrsim 1$, λ_z^w structures are also smaller than Kolmogorov scales. In the VSL, $l_C < \lambda_z^w$ in general.

Analysis of inter-component energy transfer Φ_{ii} shows that energy extraction by $\overline{u'^2}$ is more sensitive to stable stratification than $\overline{v'^2}$ or $\overline{w'^2}$. Comparison of the various terms in Φ_{ii} suggests there are changes in the directivity (or preferred alignment angles) of the vortical structures in

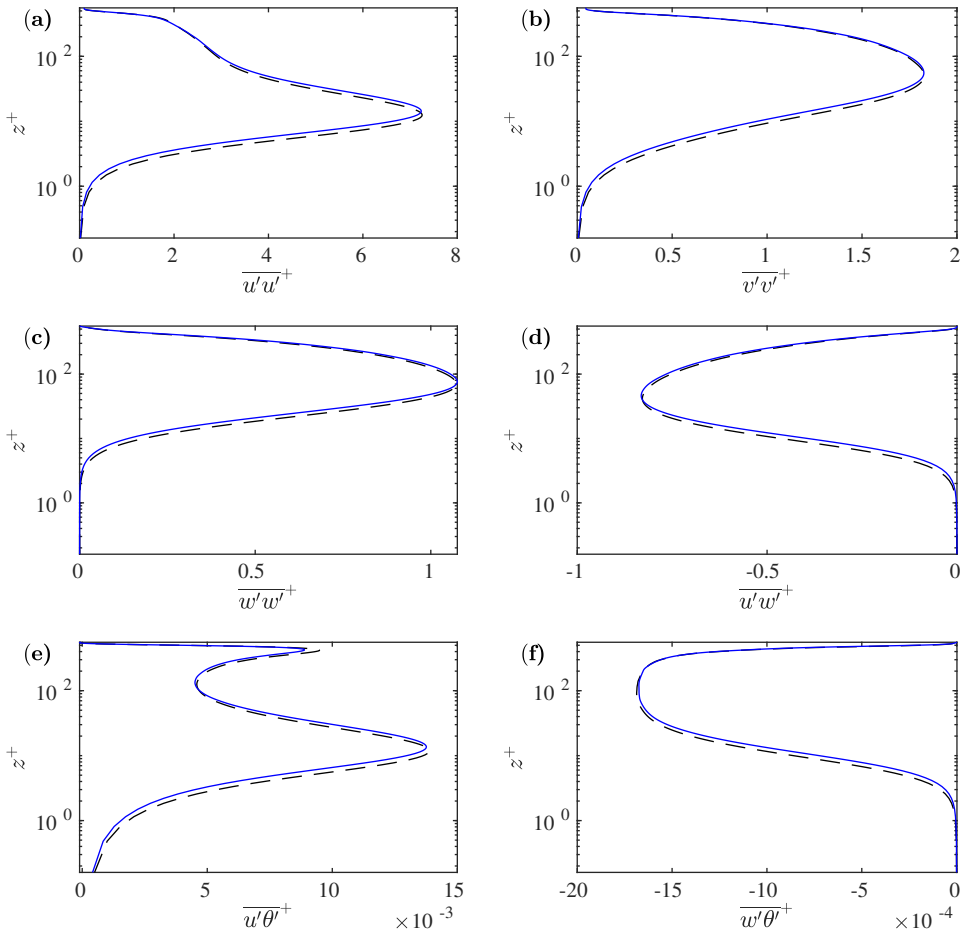

FIG. 19. Computational domain size effect on (a) $\overline{u'^2}$, (b) $\overline{v'^2}$, (c) $\overline{w'^2}$, (d) $\overline{u'w'}$, (e) $\overline{u'\theta'}$, and (f) $\overline{w'\theta'}$. Line colors are similar to Fig. 18

the near-wall region with stratification. This will be investigated in a future study.

Quasi-stationary wall turbulence under strong bottom cooling responds to the entrainment of heat from the upper boundary in a manner similar to weakly stratified turbulence with bottom cooling that has been initialized from the neutrally stratified case. However, in the quasi-stationary state, this entrainment of heat significantly affects the mean flow characteristics of the outer layer with minimal change on turbulence of the inner layer.

The effect of domain size on the results was also considered by running an additional simulation on a large domain. It was shown that mean velocity and buoyancy frequency can be accurately represented in the lower half of the channel using the smaller domain size. In the upper half, mean flow and buoyancy frequency slightly deviate from larger domain simulations. However, and consistent with studies of unstratified wall-bounded turbulence [55], one-point second-order statistics are accurately represented on a domain size of $L_x = 2\pi$, $L_y = \pi$. Although the mechanisms that are involved in the balance of TKE have been discussed here,

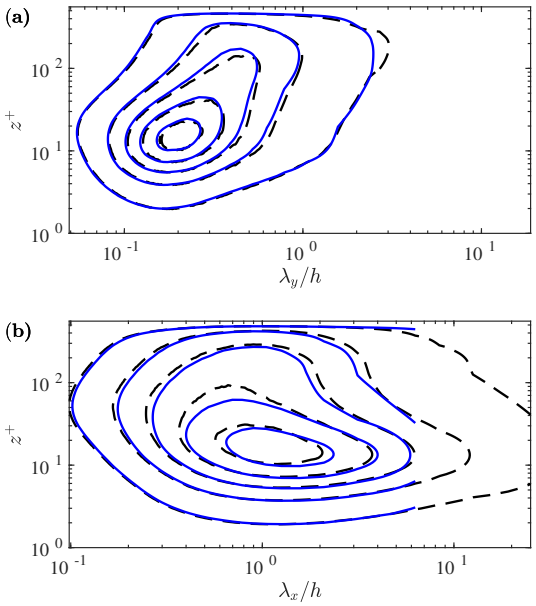

FIG. 20. Computational domain size effect on (a) spanwise pre-multiplied energy spectrum and (b) streamwise pre-multiplied energy spectrum. Line colors are similar to Fig. 18. Contours are plotted at the level of (0.1, 0.3, 0.5, 0.7, 0.9) of maximum values of energy spectrum.

the cascade of kinetic energy in strongly stable stratified wall turbulence remains an open question that will be addressed in future work.

ACKNOWLEDGMENTS

The authors are grateful to Dr. Ping He, who provided valuable assistance during the code development stage. This research was enabled in part by support provided by the Shared Hierarchical Academic Research Computing Network (SHARCNET), Compute/Calcul Canada, the Natural Sciences and Engineering Research Council of Canada (KAS: Grant No. RGPIN-418344-2012; and MLW: Grant No. RGPIN-386456-2015), and the Canadian Foundation for Innovation.

Appendix A: Reynolds stresses transport equations

The budget of Reynolds stresses are governed by [14]:

$$\frac{\partial}{\partial t}\overline{u_i'u_j'} + \overline{u_k}\frac{\partial}{\partial x_k}\overline{u_i'u_j'} = \mathrm{P_{ij}} + \mathrm{T_{ij}} + \Phi_{\mathrm{ij}} + \mathrm{D_{ij}} + \epsilon_{\mathrm{ij}} + \mathrm{B_{ij}}, \tag{A1}$$

where

$$\mathrm{P_{ij}} = -\left(\overline{u_i'u_k'}\frac{\partial \overline{u_j}}{\partial x_k} + \overline{u_j'u_k'}\frac{\partial \overline{u_i}}{\partial x_k}\right), \tag{A2}$$

$$\mathrm{T_{ij}} = -\frac{\partial \overline{u_i'u_j'u_k'}}{\partial x_k},$$

$$\Pi_{\mathrm{ij}} = -\left(\frac{\partial \overline{p'u_i'}}{\partial x_j} + \frac{\partial \overline{p'u_j'}}{\partial x_i}\right),$$

$$\Phi_{\mathrm{ij}} = \overline{\left(p'\frac{\partial u_i'}{\partial x_j} + p'\frac{\partial u_j'}{\partial x_i}\right)},$$

are production, turbulent transport, pressure-transport, pressure-strain, and

$$\mathrm{D_{ij}} = \frac{1}{Re_\tau}\frac{\partial^2 \overline{u_i'u_j'}}{\partial x_k \partial x_k}, \tag{A3}$$

$$\epsilon_{\mathrm{ij}} = -\frac{2}{Re_\tau}\overline{\frac{\partial u_i'}{\partial x_k}\frac{\partial u_j'}{\partial x_k}},$$

$$\mathrm{B_{ij}} = Ri_\tau\left(\overline{u_i'\theta'}\delta_{j3} + \overline{u_j'\theta'}\delta_{i3}\right),$$

are viscous diffusion, viscous dissipation, and buoyancy. The buoyancy terms are called buoyancy destruction if they are negative. The budget equation for TKE is similar to (A1) with $i = j$. Note that, in the TKE budget, we refer to B as buoyant destruction, since it is generally negative.

[1] L. Ran, Z. Deng, X. Xu, P. Yan, W. Lin, Y. Wang, P. Tian, P. Wang, W. Pan, and D. Lu, Vertical profiles of black carbon mea-

sured by a micro-aethalometer in summer in the north china plain, Atmospheric Chemistry and Physics **16**, 10441 (2016).

[2] M. Abkar and F. Porté-Agel, The effect of free-atmosphere stratification on boundary-layer flow and power output from very large wind farms, Energies **6**, 2338 (2013).

[3] G. Brethouwer, Y. Duguet, and P. Schlatter, Turbulent-–laminar coexistence in wall flows with coriolis, buoyancy or lorentz forces, Journal of Fluid Mechanics **704**, 137–172 (2012).

[4] A. Atoufi, K. A. Scott, and M. L. Waite, Wall turbulence response to surface cooling and formation of strongly stable stratified boundary layers, Physics of Fluids **31**, 085114 (2019).

[5] P. He, A high order finite difference solver for massively parallel simulations of stably stratified turbulent channel flows, Computers & Fluids **127**, 161 (2016).

[6] L. Mahrt, Stably stratified atmospheric boundary layers, Annual Review of Fluid Mechanics **46**, 23 (2014).

[7] F. Zonta and A. Soldati, Stably-stratified wall-bounded turbulence, Applied Mechanics Reviews 10.1115/1.4040838 (2018).

[8] O. Flores and J. J. Riley, Analysis of turbulence collapse in the stably stratified surface layer using direct numerical simulation, Boundary-Layer Meteorology **139**, 241 (2011).

[9] M. García-Villalba and J. C. del Álamo, Turbulence modification by stable stratification in channel flow, Physics of Fluids **23**, 045104 (2011).

[10] L. Mahrt, Microfronts in the nocturnal boundary layer, Quarterly Journal of the Royal Meteorological Society **145**, 546 (2019).

[11] F. Zonta, M. Onorato, and A. Soldati, Turbulence and internal waves in stably-stratified channel flow with temperature-dependent fluid properties, Journal of Fluid Mechanics **697**, 175–203 (2012).

[12] J. Huang and E. Bou-Zeid, Turbulence and vertical fluxes in the stable atmospheric boundary layer. part i: A large-eddy simulation study, Journal of the Atmospheric Sciences **70**, 1513 (2013).

[13] O. Williams, T. Hohman, T. Van Buren, E. Bou-Zeid, and A. J. Smits, The effect of stable thermal stratification on turbulent boundary layer statistics, Journal of Fluid Mechanics **812**, 1039–1075 (2017).

[14] R. P. Garg, J. H. Ferziger, S. G. Monismith, and J. R. Koseff, Stably stratified turbulent channel flows. i. stratification regimes and turbulence suppression mechanism, Physics of Fluids **12**, 2569 (2000).

[15] V. Armenio and S. Sarkar, An investigation of stably stratified turbulent channel flow using large-eddy simulation, Journal of Fluid Mechanics **459**, 1–42 (2002).

[16] J. R. Taylor, S. Sarkar, and V. Armenio, Large eddy simulation of stably stratified open channel flow, Physics of Fluids **17**, 116602 (2005).

[17] N. Williamson, S. W. Armfield, M. P. Kirkpatrick, and S. E. Norris, Transition to stably stratified states in open channel flow with radiative surface heating, Journal of Fluid Mechanics **766**, 528–555 (2015).

[18] S. Lovecchio, F. Zonta, and A. Soldati, Influence of thermal stratification on the surfacing and clustering of floaters in free surface turbulence, Advances in Water Resources **72**, 22 (2014).

[19] O. Flores and J. J. Riley, Energy balance in stably-stratified, wall-bounded turbulence, in *Mixing and Dispersion in Flows Dominated by Rotation and Buoyancy*, edited by H. J. Clercx and G. F. Van Heijst (Springer International Publishing, Cham, 2018) pp. 89–99.

[20] P. Davidson, Y. Kaneda, and K. Sreenivasan, *Ten Chapters in Turbulence* (Cambridge University Press, 2012).

[21] R. J. Adrian, Hairpin vortex organization in wall turbulence, Physics of Fluids **19**, 041301 (2007).

[22] J. M. M. Donda, I. G. S. van Hooijdonk, A. F. Moene, H. J. J. Jonker, G. J. F. van Heijst, H. J. H. Clercx, and B. J. H. van de Wiel, Collapse of turbulence in stably stratified channel flow: a transient phenomenon, Quarterly Journal of the Royal Meteorological Society **141**, 2137 (2015).

[23] J. M. M. Donda, I. G. S. van Hooijdonk, A. F. Moene, G. J. F. van Heijst, H. J. H. Clercx, and B. J. H. van de Wiel, The maximum sustainable heat flux in stably stratified channel flows, Quarterly Journal of the Royal Meteorological Society **142**, 781 (2016).

[24] Y. Ohya, D. E. Neff, and R. N. Meroney, Turbulence structure in a stratified boundary layer under stable conditions, Boundary-Layer Meteorology **83**, 139 (1997).

[25] S. H. Derbyshire, Nieuwstadt's stable boundary layer revisited, Quarterly Journal of the

Royal Meteorological Society **116**, 127 (1990).
[26] J. C. Wyngaard, *Turbulence in the Atmosphere* (Cambridge University Press, 2010).
[27] R. B. Stull, *An Introduction to Boundary Layer Meteorology*, Vol. 13 (Springer Science & Business Media, 2012).
[28] G. Blaisdell, E. Spyropoulos, and J. Qin, The effect of the formulation of nonlinear terms on aliasing errors in spectral methods, Applied Numerical Mathematics **21**, 207 (1996).
[29] J. Kim and P. Moin, Application of a fractional-step method to incompressible navier-stokes equations, Journal of Computational Physics **59**, 308 (1985).
[30] I. G. S. van Hooijdonk, J. M. M. Donda, H. J. H. Clercx, F. C. Bosveld, and B. J. H. van de Wiel, Shear capacity as prognostic for nocturnal boundary layer regimes, Journal of the Atmospheric Sciences **72**, 1518 (2015).
[31] T. M. Dillon and D. R. Caldwell, The Batchelor spectrum and dissipation in the upper ocean, Journal of Geophysical Research: Oceans **85**, 1910 (1980).
[32] M. Lesieur, *Turbulence in Fluids*, 4th ed. (Springer, 2008).
[33] P. A. Davidson, *Turbulence in Rotating, Stratified and Electrically Conducting Fluids* (Cambridge University Press, 2013).
[34] M. L. Waite, Direct numerical simulations of laboratory-scale stratified turbulence, in *Modeling Atmospheric and Oceanic Flows: Insights from Laboratory Experiments and Numerical Simulations* (Wiley, 2014) pp. 159–175.
[35] M. L. Waite and P. Bartello, Stratified turbulence dominated by vortical motion, Journal of Fluid Mechanics **517**, 281–308 (2004).
[36] F. T. M. Nieuwstadt, Direct numerical simulation of stable channel flow at large stability, Boundary-Layer Meteorology **116**, 277 (2005).
[37] J. W. Miles, On the stability of heterogeneous shear flows, Journal of Fluid Mechanics **10**, 496–508 (1961).
[38] L. N. Howard, Note on a paper of John W. Miles, Journal of Fluid Mechanics **10**, 509–512 (1961).
[39] H. Tennekes and J. L. Lumley, *A First Course in Turbulence* (MIT press, 1972).
[40] P. Davidson, *Turbulence: An introduction for Scientists and Engineers*, 2nd ed. (Oxford University Press, USA, 2015).
[41] J. W. Brooke and T. J. Hanratty, Origin of turbulence-producing eddies in a channel flow, Physics of Fluids A: Fluid Dynamics **5**, 1011 (1993).
[42] P. Holmes, J. L. Lumley, G. Berkooz, and C. W. Rowley, *Turbulence, Coherent Structures, Dynamical Systems and Symmetry*, 2nd ed., Cambridge Monographs on Mechanics (Cambridge University Press, 2012).
[43] S. Shah and E. Bou-Zeid, Rate of decay of turbulent kinetic energy in abruptly stabilized ekman boundary layers, Phys. Rev. Fluids **4**, 074602 (2019).
[44] J. J. Riley and M.-P. Lelong, Fluid motions in the presence of strong stable stratification, Annual Review of Fluid Mechanics **32**, 613 (2000).
[45] J. Jiménez, Near-wall turbulence, Physics of Fluids **25**, 10.1063/1.4824988 (2013).
[46] B. Dubrulle, Beyond Kolmogorov cascades, Journal of Fluid Mechanics **867**, P1 (2019).
[47] A. W. Vreman and J. G. M. Kuerten, Statistics of spatial derivatives of velocity and pressure in turbulent channel flow, Physics of Fluids **26**, 085103 (2014).
[48] T. H. Ellison, Turbulent transport of heat and momentum from an infinite rough plane, Journal of Fluid Mechanics **2**, 456–466 (1957).
[49] B. D. Mater, S. M. Schaad, and S. K. Venayagamoorthy, Relevance of the Thorpe length scale in stably stratified turbulence, Physics of Fluids **25**, 076604 (2013).
[50] T. M. Dillon, Vertical overturns: A comparison of Thorpe and Ozmidov length scales, Journal of Geophysical Research: Oceans **87**, 9601 (1982).
[51] S. B. Pope, *Turbulent flows* (Cambridge University Press, 2000).
[52] P. A. Durbin and B. P. Reif, *Statistical Theory and Modeling for Turbulent Flows* (John Wiley & Sons, 2011).
[53] J. Jiménez, Cascades in wall-bounded turbulence, Annual Review of Fluid Mechanics **44**, 27 (2012).
[54] J. Jiménez, Near-wall turbulence, Physics of Fluids **25**, 101302 (2013).
[55] A. Lozano-Durán and J. Jiménez, Effect of the computational domain on direct simulations of turbulent channels up to $Re_\tau = 4200$, Physics of Fluids **26**, 011702 (2014).
[56] L. Quan, E. Ferrero, and F. Hu, Relating statistical moments and entropy in the stable boundary layer, Physica A: Statistical Mechanics and its Applications **391**, 231 (2012).
[57] T. Tatsumi and G. I. Taylor, The theory of decay process of incompressible isotropic turbulence, Proceedings of the Royal Society of

London. Series A. Mathematical and Physical Sciences **239**, 16 (1957).

[58] P. Vedula, R. D. Moser, and P. S. Zandonade, Validity of quasinormal approximation in turbulent channel flow, Physics of Fluids **17**, 055106 (2005).

[59] O. Zeman and J. L. Lumley, Modeling buoyancy driven mixed layers, Journal of the Atmospheric Sciences **33**, 1974 (1976).

[60] A. Lozano-Durán and J. Jiménez, Time-resolved evolution of coherent structures in turbulent channels: characterization of eddies and cascades, Journal of Fluid Mechanics **759**, 432–471 (2014).

[61] J. Jiménez and P. Moin, The minimal flow unit in near-wall turbulence, Journal of Fluid Mechanics **225**, 213–240 (1991).

[62] O. Flores and J. Jiménez, Hierarchy of minimal flow units in the logarithmic layer, Physics of Fluids **22**, 071704 (2010).

[63] A. A. Townsend, Equilibrium layers and wall turbulence, Journal of Fluid Mechanics **11**, 97–120 (1961).

[64] P. Bradshaw, 'inactive' motion and pressure fluctuations in turbulent boundary layers, Journal of Fluid Mechanics **30**, 241–258 (1967).